

# A Multifunctional Origami Patch for Minimally Invasive Tissue Sealing

Sarah J. Wu, Hyunwoo Yuk,\* Jingjing Wu, Christoph S. Nabzdyk, and Xuanhe Zhao\*

For decades, bioadhesive materials have garnered great attention due to their potential to replace sutures and staples for sealing tissues during minimally invasive surgical procedures. However, the complexities of delivering bioadhesives through narrow spaces and achieving strong adhesion in fluid-rich physiological environments continue to present substantial limitations to the surgical translation of existing sealants. In this work, a new strategy for minimally invasive tissue sealing based on a multilayer bioadhesive patch, which is designed to repel body fluids, to form fast, pressure-triggered adhesion with wet tissues, and to resist biofouling and inflammation is introduced. The multifunctional patch is realized by a synergistic combination of three distinct functional layers: i) a microtextured bioadhesive layer, ii) a dynamic, blood-repellent hydrophobic fluid layer, and iii) an antifouling zwitterionic nonadhesive layer. The patch is capable of forming robust adhesion to tissue surfaces in the presence of blood, and exhibits superior resistance to bacterial adhesion, fibrinogen adsorption, and in vivo fibrous capsule formation. By adopting origami-based fabrication strategies, it is demonstrated that the patch can be readily integrated with a variety of minimally invasive end effectors to provide facile tissue sealing in ex vivo porcine models, offering new opportunities for minimally invasive tissue sealing in diverse clinical scenarios.

surgical skill, making it disadvantageous during emergency scenarios. Meanwhile, surgical staplers are associated with an increasing number of adverse events caused by complications, such as staple malformations and stapler misfirings.<sup>[1]</sup> Moreover, both sutures and staples can be mechanically damaging to tissues and are prone to dehiscence, leakage, and inflammation.<sup>[2,3]</sup> Associated postoperative complications, such as anastomotic leaks and fibrous adhesion formation with surrounding organs, can result in devastating clinical consequences for patients and often require subsequent readmission surgeries to achieve definitive surgical repair.<sup>[4,5]</sup> The challenges associated with sutures and staples are further amplified in minimally invasive settings, during which the use of endoscopic equipment typically limits visualization, depth perception, range of motion, and haptic feedback.<sup>[6]</sup> Thus, although recent advances in surgical equipment have focused on evolving surgery toward less invasive techniques, tissue sealing remains a prevailing challenge.

The ability to connect tissues is one of the cornerstones of general surgery. To this end, the traditional strategies of applying mechanical fasteners (i.e., sutures and staples) remain the current standards for sealing and repairing tissues in both open and minimally invasive surgery. However, these modalities have inherent drawbacks. Suturing entails complex manipulations which are time-consuming and require a high level of

In light of these shortcomings, bioadhesive materials have gained great attention as promising alternatives or adjuncts to sutures and staples for closing defects and attaching devices to organs.<sup>[2,3,7–14]</sup> However, most existing bioadhesives struggle to meet the functional requirements needed for practical use in minimally invasive surgery (Figure S1 and Table S1, Supporting Information). Most bioadhesives are available in the forms of liquids and glues, which can be easily displaced or diluted in dynamic and wet physiological environments.<sup>[3]</sup> Additionally, many bioadhesives suffer from contamination in the presence of body fluids such as blood and mucus, which render them ineffective before they can be maneuvered to the target tissues.<sup>[15]</sup> Several bioadhesives incorporate external-stimuli-based adhesion activation such as ultraviolet (UV)-light crosslinking to offer improved controllability.<sup>[16,17]</sup> However, the requirement of external activation sources can hinder their usability by introducing additional complex and time-consuming procedures. Furthermore, many bioadhesive precursors solidify into rigid polymers that are less stretchable and much stiffer than the adhered soft tissues, resulting in an adhesive-to-host compliance mismatch.<sup>[18]</sup> These limitations are often associated with relatively low adhesion strength and slow adhesion formation.<sup>[13,19]</sup> Additional clinical concerns include inflammatory

S. J. Wu, Dr. H. Yuk, Dr. J. Wu, Prof. X. Zhao  
 Department of Mechanical Engineering  
 Massachusetts Institute of Technology  
 Cambridge, MA 02139, USA  
 E-mail: hyunwoo@mit.edu; zhaox@mit.edu

Prof. C. S. Nabzdyk  
 Department of Anesthesiology and Perioperative Medicine  
 Mayo Clinic  
 Rochester, MN 55905, USA

Prof. X. Zhao  
 Department of Civil and Environmental Engineering  
 Massachusetts Institute of Technology  
 Cambridge, MA 02139, USA

 The ORCID identification number(s) for the author(s) of this article can be found under <https://doi.org/10.1002/adma.202007667>.

DOI: 10.1002/adma.202007667

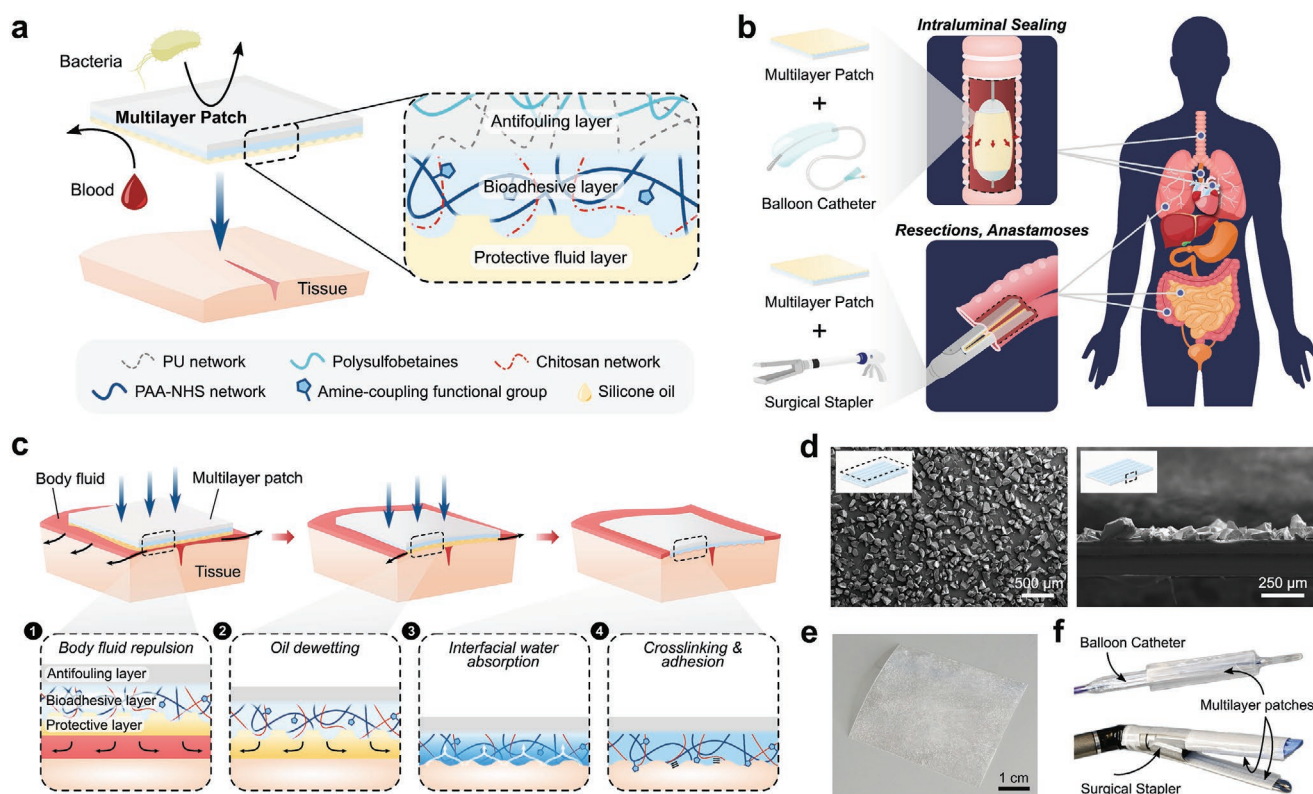


**Figure 1.** a) Illustrated schematic of the multilayer composition of the bioadhesive patch. The patch comprises a textured bioadhesive fused with an antifouling polymer layer on the non-adherent side, and is wetted with a hydrophobic fluid layer on the adherent side to repel body fluids. b) Illustrated exemplary minimally invasive surgical applications of the multilayer patch via balloon catheters for intraluminal sealing of tube-shaped organs and structures, and surgical staplers for linear seals in resections and anastomoses. c) Schematic of the adhesion mechanism of the multilayer patch. (1) As the patch is maneuvered toward the tissue, the hydrophobic protective layer repels blood and prevents contamination of the bioadhesive layer. (2) Application of pressure exceeding 77.5 kPa drives dewetting of the oil from the bioadhesive layer. (3) The bioadhesive layer makes contact with the tissue surface and absorbs interfacial water immediately, forming temporary crosslinks. (4) Covalent bonds form between NHS ester functional groups in the bioadhesive layer for stable, long term adhesion. d) Scanning electron microscopy images of a top-view (left) and a side-view (right) of the microtextured surface of the bioadhesive layer. e) Photograph of the assembled multilayer patch. f) Multilayer patches loaded on a balloon catheter and surgical stapler.

responses, such as postoperative adhesion formation, and perioperative infectious complications.<sup>[3]</sup>

Here, we introduce a new strategy for tissue sealing and repair based on a multilayer tissue sealing patch, which synergistically combines three core functionalities to address the above-mentioned limitations (**Figure 1**): body fluid resistance, strong on-demand adhesion to wet tissues, and antifouling behavior. To achieve these properties, the patch integrates three distinct functional layers: i) a microtextured bioadhesive layer, ii) a dynamic, blood-repellent hydrophobic fluid layer, and iii) an antifouling zwitterionic nonadhesive layer. Notably, the material properties of the multilayer patch make it amenable to origami-inspired fabrication methods which endow it with a high degree of customizability. This ability to adopt customized form factors enables surgical application through a variety of deployment mechanisms driven by different surgical end effectors, offering a promising solution to a wide range of clinical indications (**Figure 1b**).

The multilayer composition of the tissue sealing patch is illustrated in **Figure 1a**. The patch comprises a bioadhesive layer sandwiched between an infused hydrophobic fluid layer and an antifouling nonadhesive layer. The hydrophobic fluid

layer serves as a protective barrier which prevents the adhesive layer from becoming contaminated in the presence of body fluids by repelling blood and other immiscible contaminants. Microtexturing of the bioadhesive interface promotes the infiltration of the fluid layer through stabilizing capillary forces.<sup>[20,21]</sup> Here, silicone oil has been employed as the hydrophobic fluid agent due to its chemical stability, established internal use as a lubricant for medical devices, and favorable wettability to the bioadhesive material.<sup>[22]</sup> Due to the contributing effect of substrate microstructures, the hydrophobic fluid layer can be stably maintained during navigation through fluid-rich environments, preserving the adhesive capacity of the underlying bioadhesive layer. Only under sufficient pressure does the textured bioadhesive surface undergo shear-driven dewetting, allowing for triggered deprotection of the bioadhesive layer. The pressure threshold for dewetting can be actively applied by pressing against tissue surfaces in order to: 1) expel the oil and 2) allow the then-exposed bioadhesive material to adhere to the tissue (**Figure 1c**).

For the bioadhesive layer, we employ a double network material comprised of poly(acrylic acid) grafted with *N*-hydroxysuccinimide ester (PAA-NHS ester) and chitosan (**Figure 1a**).<sup>[13]</sup>

This bioadhesive material forms fast and strong adhesion to wet tissues by adopting a dry-crosslinking mechanism. When the dry bioadhesive layer comes into contact with a wet tissue surface, it quickly absorbs the interfacial water and forms physical bonds (e.g., hydrogen bonds) within seconds (Figure 1c).<sup>[13,23]</sup> Subsequent formation of covalent bonds between the NHS ester groups and primary amine groups on the tissue surface further improves the adhesion strength and stability of the bioadhesive. Upon hydration and adhesion on wet tissues, the bioadhesive layer becomes a hydrogel with mechanical compliance and stretchability comparable to those of soft tissues.<sup>[13,24]</sup> To introduce microtexture into the adhesive surface of the bioadhesive layer, microparticles of the bioadhesive material were produced by cryogenic grinding and embedded into the flat surface of a bioadhesive substrate. A 3D reconstruction of confocal microscopy images taken at the interface of the microtextured bioadhesive (prepared using green-fluorescent fluorescein-labeled chitosan) adhered to a gelatin hydrogel tissue phantom (prepared using red-fluorescent Rhodamine-Red-labeled microbeads) shows the conformal adhesion interface between the microtextured bioadhesive and the gelatin hydrogel (Figure S2b, Supporting Information).

To mitigate biofouling and postoperative inflammation, we integrate a zwitterionic-interpenetrated elastomer layer on the nonadhesive face of the patch (Figure 1a). Zwitterionic polymers have been found to have excellent antifouling properties.<sup>[25–29]</sup> Their unique ability to resist foulant adsorption is attributed to the presence of cationic and anionic groups in net neutral polymer chains, which promote the formation of a tight hydration shell while minimally disrupting the hydrogen-bonding structure of free water molecules (Figure 3a).<sup>[25,28]</sup> Disturbance of this hydration shell carries a high energy cost which precludes the surface adsorption of bacteria and biomolecules associated with inflammatory responses such as infection, blood coagulation, and postoperative adhesion formation. However, zwitterionic hydrogels typically suffer from poor mechanical properties such as low toughness and stretchability, which can be detrimental for their long-term robustness and stability in dynamic physiological environments.<sup>[30]</sup> To achieve a tough and stretchable antifouling layer for the patch, we interpenetrate zwitterionic polymers (i.e., poly(sulfobetaine methacrylate) (PSBMA)) into the surface of a thin film of hydrophilic polyurethane (PU) to synergistically combine the antifouling capacity of the zwitterionic moieties and the mechanical robustness of PU (Figure S3, Supporting Information).<sup>[31]</sup> The resultant zwitterionic-interpenetrated PU layer exhibits superior mechanical properties (fracture toughness around  $420 \text{ J m}^{-2}$  and stretchability over 3.5 times of the original length) compared to pure zwitterionic PSBMA hydrogels (fracture toughness around  $0.35 \text{ J m}^{-2}$  and stretchability less than 1.5 times of the original length) (Figure 3c; and Figure S4, Supporting Information). To verify the presence of polysulfobetaines in the treated PU film, the surface was characterized by Fourier transform infrared (FTIR) spectroscopy (Figure 3b). Compared to pristine PU, the FTIR spectrum for the zwitterionic-interpenetrated PU shows strong absorbance peaks at  $1020$  and  $1180 \text{ cm}^{-1}$ , which correspond to vibrations of the sulfonate group ( $-\text{SO}_3^-$ ) present in the sulfobetaine moiety (Figure 3b).<sup>[30,31]</sup> The zwitterionic layer is integrated with the bioadhesive layer by using a thin coat of

hydrophilic PU solution to bond the two layers at the interface. The fully integrated multilayer patch takes the form of a thin and flexible polymer film in the dry state (Figure 1e), while it becomes a highly stretchable (stretchability over 5.5 times of the original length), soft (shear modulus around  $70 \text{ kPa}$ ), and tough (fracture toughness around  $2100 \text{ J m}^{-2}$ ) hydrogel in the swollen state after forming adhesion on wet tissues (Figure S5, Supporting Information).

To evaluate the protective capacity of the hydrophobic fluid layer, we exposed samples of the patch with and without silicone oil to blood and compared their fouling behaviors (Figure 2a). When submerged in a porcine blood bath, the patch without the silicone oil layer is immediately wetted by the blood and loses its adhesive capability, whereas the patch with the protective silicone oil layer resists blood contamination and remains intact (Figure 2a; and Figure S6, Supporting Information). To further investigate the effect of surface microtexture on the stability of the fluid layer, we vigorously shook multilayer patches with flat and microtextured bioadhesive surfaces in a porcine blood bath. While the multilayer patch with a flat bioadhesive surface shows substantial blood contamination after shaking, the patch comprising a microtextured surface exhibits robust protection of the bioadhesive layer against vigorous blood flow (Figure 2b; and Movie S1, Supporting Information), supporting the significance of the microtextured design of the bioadhesive layer in order to achieve stable contaminant-repellent properties.<sup>[20]</sup>

As the patch is brought in contact with a tissue substrate, applying pressure drives expulsion of the hydrophobic fluid layer from between the two solid surfaces. The exposed bioadhesive layer is then able to adhere to the tissue surface via the dry-crosslinking mechanism described above (Figure 1c). However, during this pressure-driven dewetting of the bioadhesive layer, it is possible for residual interfacial blood and oil to coalesce and remain entrapped at the interface, forming small nonadhered regions (Figures S8–S10, Supporting Information). If substantial pockets of blood or oil become entrapped at the interface, the strength of the adhesive bond between the patch and the tissue can deteriorate. The amount of entrapped fluid is contingent on the pressure applied during compression of the multilayer patch against the tissue surface. To determine the optimal pressure conditions for removing interfacial blood and maximizing the area of adhesion, we quantified the amount of residual blood entrapped between patches and gelatin hydrogel tissue phantoms which were adhered under varying applied pressures while covered with porcine blood (Figures S7a,b and S8, Supporting Information). We also measured the adhesive shear strength of patches adhered to blood-covered porcine skin tissues which were adhered under the same varying pressures (Figure S7c and S10, Supporting Information). As the applied pressure increases, the area of entrapped blood decreases, while the adhesive shear strength increases (Figure S7, Supporting Information). When the applied pressure exceeds  $77.5 \text{ kPa}$ , the amount of entrapped blood and the adhesive shear strength both reach plateau values, indicating that a threshold pressure of  $77.5 \text{ kPa}$  can effectively repel most of the interfacial blood and activate optimal adhesion of the multilayer patch. Notably, this level of pressure (i.e., around  $100 \text{ kPa}$ ) can be readily applied by surgical end effectors, such as staplers and balloons.<sup>[33–35]</sup>



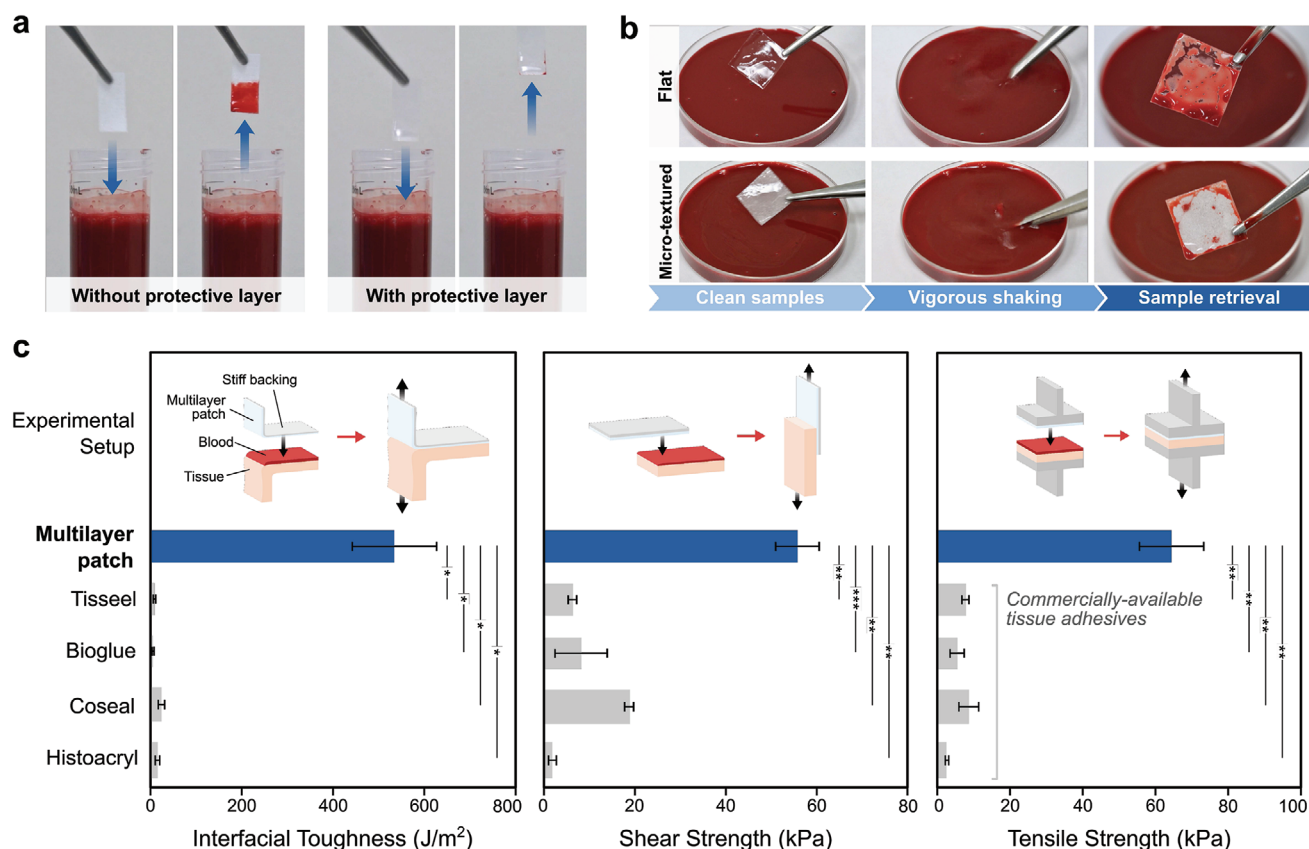


**Figure 2.** a) Photographs of multilayer patches with and without the hydrophobic fluid layer before and after submerging in porcine blood. b) Photographs of the multilayer patches with flat and microtextured bioadhesive layers before and after vigorously shaking in a porcine blood bath. The multilayer patch containing a microtextured bioadhesive layer exhibits greater stability and blood-repellent capacity of the hydrophobic fluid layer. c) Comparison of adhesion performances of the multilayer patch and various commercially available tissue adhesives, adhered to porcine skin coated with porcine blood. Values represent the mean and the standard deviation ( $n = 3$ ).  $P$  values are determined by a Student's  $t$ -test; ns, not significant ( $p > 0.05$ ); \*  $p \leq 0.05$ ; \*\*  $p \leq 0.01$ ; \*\*\*  $p \leq 0.001$ .

To quantitatively evaluate the ability of the multilayer patch to form adhesion in blood, we adhered samples of the patch with porcine skin tissues submerged in a blood bath using an applied pressure of 77.5 kPa, and then performed 180° peel tests (ASTM F2256), lap-shear tests (ASTM F2255), and tensile tests (ASTM F2258) to measure the interfacial toughness, shear strength, and tensile strength of the adhered samples, respectively (Figures S11 and S12, Supporting Information). We also measured the interfacial toughness, shear strength, and tensile strength of porcine skin tissues adhered using various commercially available tissue adhesives including fibrin-based Tisseel, albumin-based Bioglue, poly(ethylene glycol) (PEG)-based Coseal, and cyanoacrylate-based Histoacryl (Figure 2c). Compared to these commercially available tissue adhesives, the multilayer patch resists blood contamination and achieves significantly higher interfacial toughness ( $536.7 \pm 93.4 \text{ J m}^{-2}$ ), shear strength ( $56.1 \pm 4.7 \text{ kPa}$ ), and tensile strength ( $65.0 \pm 8.0 \text{ kPa}$ ) (Figure 2c).

To characterize the antifouling performance of the zwitterionic layer, we investigated the patch's capability to mitigate in vitro bacterial adhesion, in vitro fibrinogen adsorption, and in vivo fibrous capsule formation (Figure 3d–j). Bacterial attachment to implanted materials can lead to biofilm formation

and surgical site infection, which cause significant patient morbidity and substantial healthcare costs due to the need for additional procedures and antimicrobial therapies. To evaluate the antimicrobial performance of the zwitterionic layer, various patches with nonadhesive faces comprised of a hydrophobic polymer (poly(dimethylsiloxane) (PDMS)), a hydrophilic polymer (pristine hydrophilic PU), and the zwitterionic-interpenetrated elastomer were incubated with a green-fluorescent protein (GFP)-expressing *Escherichia coli* (*E. coli*). After 24 h of incubation, the density of adhered *E. coli* on each surface was examined using fluorescence microscopy and measured in ImageJ (Figure 3d). In contrast to the patches featuring hydrophobic ( $\approx 1370 \text{ counts mm}^{-2}$ ) and hydrophilic nonadhesive layers ( $\approx 1360 \text{ counts mm}^{-2}$ ), the patch with the zwitterionic layer exhibits a significantly lower level of *E. coli* adhesion ( $\approx 0.9 \text{ counts mm}^{-2}$ ) (Figure 3e).

We further evaluated the antifouling performance of the zwitterionic layer in blood by evaluating its capacity to resist the adsorption of fibrinogen in porcine whole blood. Surface attachment of fibrinogen leads to the formation of a fibrin meshwork, which serves as the basis of a blood clot. Thus, the surface coverage of fibrin can indicate the potential for a biomaterial to induce platelet accumulation, activation, and thrombus



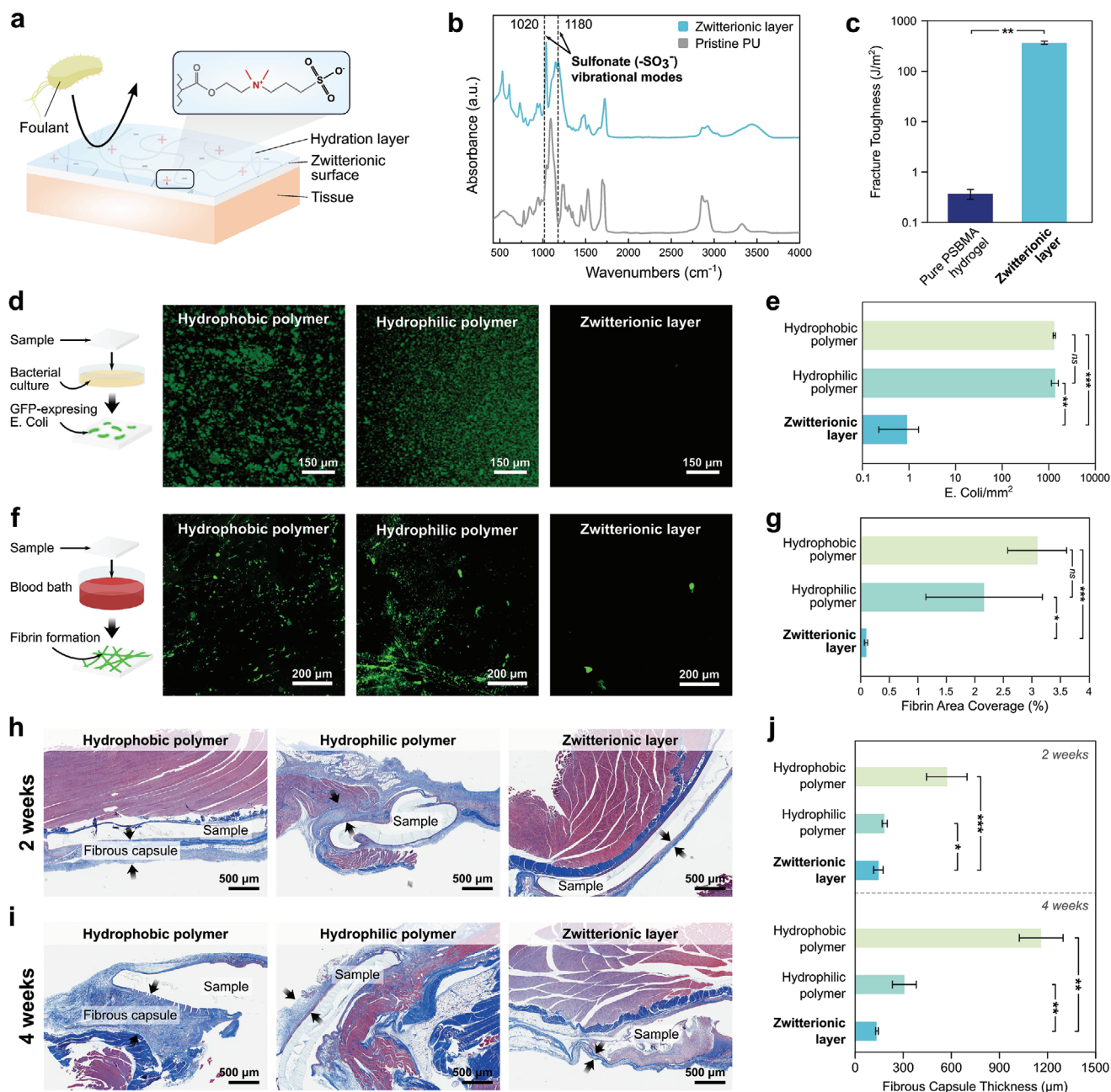


**Figure 3.** In vitro and in vivo antifouling performance of the multilayer patch. a) Illustrated depiction of the antifouling mechanism of the zwitterionic-interpenetrated elastomer. Foulant adsorption is prevented due to the formation of a tightly bound hydration layer caused by electrostatic interactions between water molecules and the charged zwitterionic polymers. b) FTIR spectra of the zwitterionic layer and unmodified pristine hydrophilic PU; peaks at 1020  $\text{cm}^{-1}$  and 1180  $\text{cm}^{-1}$  correspond to vibrational modes of the sulfonate group ( $\text{SO}_3^-$ ). c) Fracture toughness of a pure zwitterionic hydrogel (0.35  $\text{J m}^{-2}$ ) and the zwitterionic-interpenetrated elastomer layer (420  $\text{J m}^{-2}$ ). d) Representative fluorescence microscopy images of GFP-expressing *E. coli* adhered to a hydrophobic polymer (PDMS), a hydrophilic polymer (PU), and the zwitterionic layer following 24 h incubation. e) The number of adhered *E. coli* per  $\text{mm}^2$  for each substrate. f) Representative fluorescence microscopy images of fibrin network formation on a hydrophobic polymer (PDMS), a hydrophilic polymer (PU), and the zwitterionic layer after 60 min of exposure to porcine whole blood spiked with fluorescently tagged fibrinogen. g) Fibrin area coverage (%) for each substrate. h, i) Representative histological images stained with Masson's trichrome for in vivo rat dorsal subcutaneous implantation of patches with non-adhesive faces comprised of a hydrophobic polymer (PDMS, left), a hydrophilic polymer (PU, middle), and the zwitterionic layer (right) after 2 weeks (h) and 4 weeks (i). j) Fibrin capsule thickness formed around the implanted samples after in vivo implantation. Values in (c,e,g,i) represent the mean and the standard deviation ( $n = 4$ ).  $P$  values are determined by a Student's  $t$ -test; \*  $p \leq 0.05$ ; \*\*  $p \leq 0.01$ ; \*\*\*  $p \leq 0.001$ .

formation, which are undesirable for applications in which the bioadhesive interfaces with a bloodstream. Samples with non-adhesive layers comprised of a hydrophobic polymer (PDMS),

a hydrophilic polymer (pristine hydrophilic PU), and the zwitterionic-interpenetrated elastomer were submerged in a blood bath containing heparinized porcine whole blood spiked with

fibrinogen tagged with Alexa Fluor 488 following a previously reported protocol.<sup>[22,36]</sup> After 60 min of incubation, the samples were fixed and the areal coverage of fibrin was compared among the different samples. Similar to the results for bacterial adhesion, the patch with the zwitterionic layer shows significantly lower levels of fibrin deposition ( $\approx 0.1\%$  areal coverage) compared to the patches with hydrophobic ( $\approx 3.09\%$  areal coverage) and hydrophilic faces ( $\approx 2.16\%$  areal coverage) (Figure 3f,g). These results reflect a lower thrombogenic risk associated with the zwitterionic material in contact with whole blood.

To evaluate the biocompatibility and in vivo antifouling performance of the multilayer patch, we compared in vivo inflammation in rats in response to implanted patches with nonadhesive layers comprised of a hydrophobic polymer (PDMS), a hydrophilic polymer (pristine hydrophilic PU), and the zwitterionic-interpenetrated elastomer. Samples were implanted in the dorsal subcutaneous pockets of rats. At

time points of 2 and 4 weeks following implantation, the tissues were collected and fixed for histological analysis and the thickness of the fibrous capsule around each implant was measured (Figure 3h–j). The formation of a thick fibrotic encapsulation around the surgical site is highly undesirable and can result in complications, such as organ stricture and postoperative adhesions.<sup>[37,38]</sup> After 2 weeks of implantation, histological analysis shows that the patch with the zwitterionic layer exhibits a significantly thinner fibrous capsule around the patch ( $145 \pm 29 \mu\text{m}$ ) compared to the patches with hydrophobic ( $574 \pm 125 \mu\text{m}$ ) and hydrophilic polymer layers ( $185 \pm 16 \mu\text{m}$ ) (Figure 3h–j). After 4 weeks of implantation, the patch with the zwitterionic layer maintains a similar thickness of fibrous capsule around the patch ( $135 \pm 7 \mu\text{m}$ ) to the 2 week results, whereas the patches with hydrophobic ( $1163 \pm 138 \mu\text{m}$ ) and hydrophilic ( $307 \pm 73 \mu\text{m}$ ) polymer layers exhibit significantly thicker fibrous capsules than their respective 2 week results

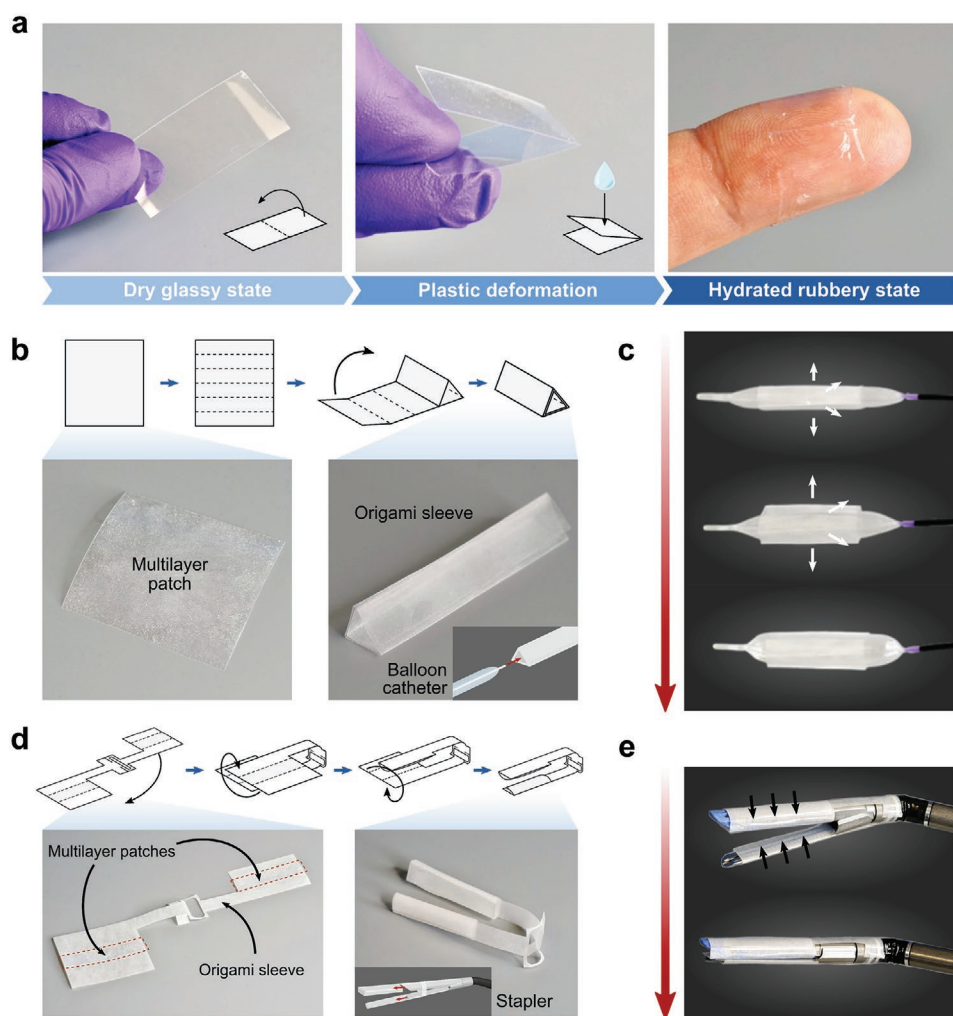


**Figure 4.** Design and assembly of the multilayer patch for various surgical end effectors. a) Photographs showing the multilayer patch in the plastically deformable dry glassy state. Upon hydration, the folded patch transitions to the rubbery state and becomes a soft conformable hydrogel. b) Origami-based design and fabrication of a triangular sleeve for integration of the multilayer patch with a balloon catheter. c) Photographs showing the deployment mechanism using an esophageal balloon catheter. Increasing inflation pressure in the balloon induces radial expansion and unfurling of the multilayer patch. d) Origami-based design and fabrication of a dual-sleeve adaptor for integration of the multilayer patch with an articulating linear stapler. The multilayer patches are denoted by the red dashed lines. e) Photographs showing the deployment mechanism using an articulating linear stapler. Actuation of the stapler compresses the anvil and cartridge units together, triggering adhesion.

(Figure 3i,j). In summary, these results suggest that the zwitterionic layer of the multilayer patch possesses favorable capacities to resist a range of perioperative and postoperative complications including bacterial adhesion, thrombus formation, and fibrotic encapsulations.

To further confirm the *in vivo* biocompatibility of the multilayer patch, histological images of the implanted samples were submitted for histological analysis and evaluated by a blinded pathologist (Figure S13, Supporting Information). The degree of inflammation at the implantation site for the zwitterionic layer-containing patch received average scores of 1.33 and 1.67 after 2 and 4 weeks, respectively, which fall within the “very mild” to “mild” inflammation range. These results indicate that the multilayer patch elicits low levels of acute and chronic inflammation. Because the bioadhesive layer is comprised of PAA-NHS ester crosslinked with biodegradable linkages and the biopolymer chitosan, it can be left to undergo enzymatic biodegradation within the body if it is intended to be implanted without recurrent surgery (Figure S14, Supporting Information).<sup>[13]</sup> The degradation rate can be tuned by changing the type of biopolymer used in the bioadhesive material (e.g., gelatin or alginate instead of chitosan) or the ratio of crosslinking agent used.

To explore the translational potential of the multilayer patch in minimally invasive surgery, we demonstrate two different deployment strategies (balloon catheter and surgical stapler) for applying the patch using existing minimally invasive surgical instruments (Figure 4). The multilayer patch can be customized to adopt diverse form factors owing to its thin, paper-like form and the material properties of its constituents. At room temperature, the dry bioadhesive layer of the patch is in the glassy state. As a result, a folded patch can maintain the folded hinges due to plastic deformation, making the patch amenable to origami-based designs (Figure 4a).<sup>[39–41]</sup> Hydration of the bioadhesive material, which occurs upon contact with wet tissues, lowers the glass transition temperature and causes the material to transit into the rubbery state. This transition releases the plastic deformation at the folded hinges, and allows the patch conform to the tissue substrate. These properties enable the patch to undertake versatile geometries to suit various end effectors, such as balloon catheters and endoscopic staplers, and to form fluid-tight seals with curved and irregular tissue surfaces.

One such minimally invasive application enabled by the multilayer patch is the endoluminal sealing of tube-shaped organs and structures (e.g., trachea, esophagus, and vessels) via balloon

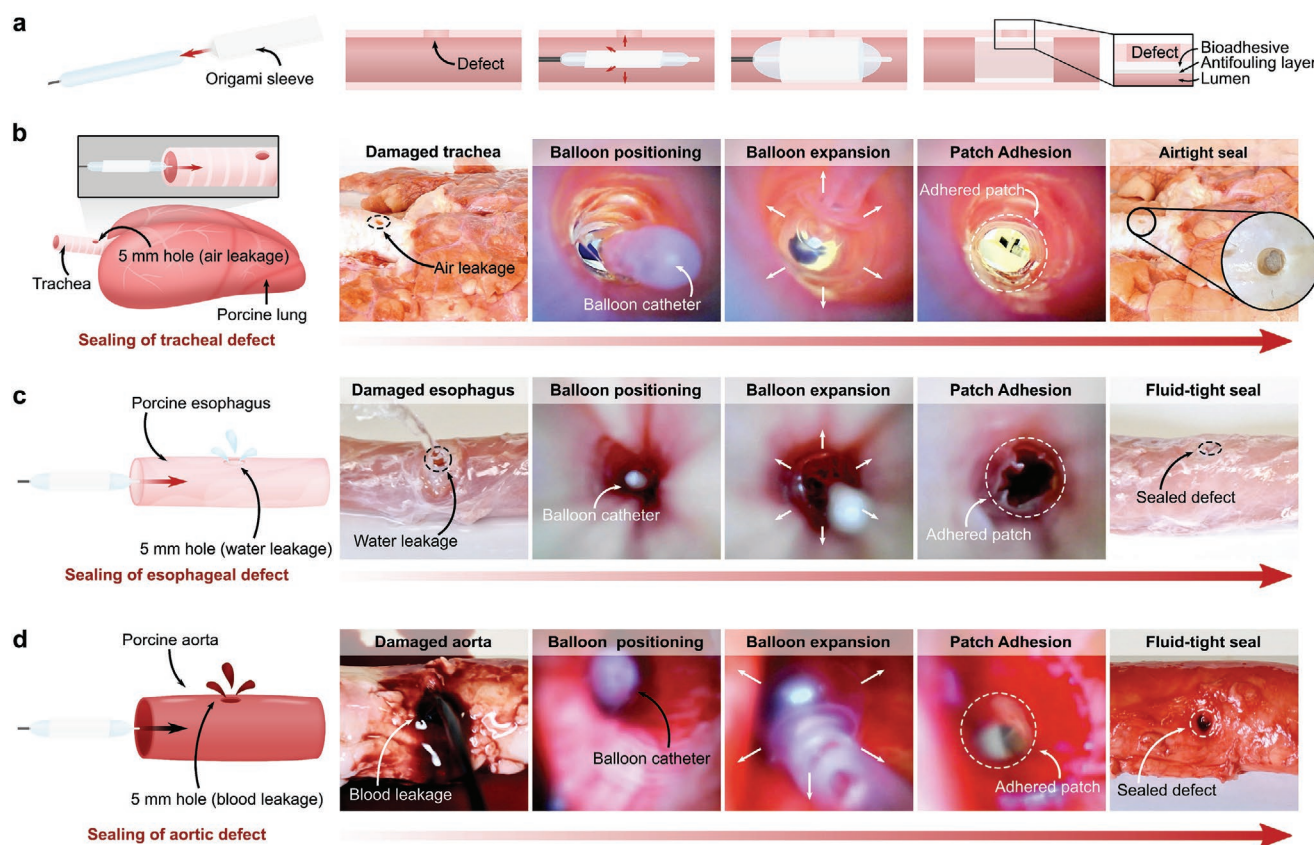


**Figure 5.** Ex vivo demonstrations of minimally invasive delivery and application of the multilayer bioadhesive patch by balloon catheters. a) Schematic illustrations of the origami patch integration and endoluminal delivery process using a balloon catheter. b) Macroscopic and endoscopic photographs of the airtight sealing of a porcine tracheal defect (5-mm hole) by the multilayer patch delivered and applied via a Foley catheter. c) Macroscopic and endoscopic photographs of the fluid-tight sealing of a porcine esophageal defect (5-mm hole) by the patch delivered and applied via an esophageal catheter. d) Macroscopic and endoscopic photographs of the fluid-tight sealing of a porcine aortic defect (5-mm hole) by the patch delivered and applied via a Foley catheter.



catheters. For balloon catheter-based delivery and application, the patch is folded into a sleeve circumscribing the uninflated balloon, with the hydrophobic fluid layer oriented outward (Figure 4b). The sleeve unfurls upon inflation of the balloon, expanding to meet the walls of the hollow organ or vessel (Figure 4c). As the inflation pressure of the balloon increases, the radial pressure exerted by the balloon compresses the patch against the tissue wall, triggering the deprotection and adhesion of the bioadhesive layer (Figure 5a). We demonstrate that the proposed concept is readily applicable to a variety of surgical sites, exemplified in ex vivo experiments in which different sizes of balloon catheters were utilized to seal defects in a porcine trachea, esophagus, and aorta. Insertion and expansion of a Foley catheter (ReliaMed) outfitted with an origami patch sleeve resulted in the airtight sealing of a porcine trachea with a 5 mm circular transmural defect, immediately restoring the inflation capability of the lungs (Figure 5b; and Movie S2, Supporting Information). Similarly, adapting the dimensions of the origami sleeve to fit an esophageal balloon catheter (Boston Scientific) enabled rapid and fluid-tight sealing of a 5 mm circular transmural defect in a porcine esophagus (Figure 5c; and Movie S3, Supporting Information). The Foley-catheter-based application method was further used to achieve hemostatic sealing of a 5 mm circular defect in an aorta (Figure 5d; and Movie S4, Supporting Information). The esophageal and aortic seals achieved using this strategy withstood the pumping of water and blood, respectively, at supraphysiological pressures over 300 mm Hg.

In addition to endoluminal sealing method using balloon catheters, we demonstrate that the multilayer patch can be integrated with an articulating endoscopic stapler (Ethicon) to provide a linear seal (Figure 6). This strategy of tissue repair could be useful for broader surgical applications, such as

anastomoses and resections. To enable stapler-based minimally invasive delivery, the multilayer patch is cut into various-sized strips and loaded in a folded origami sleeve designed to wrap around the anvil and cartridge units of the stapler (Figure 6a). Once the stapler jaws are positioned around the site of the tissue injury, actuation of the stapler compresses the multilayer patches against the tissue surface, triggering adhesion and sealing of the defect (Figure 6a). Using this method, the multilayer patch achieved rapid, fluid-tight sealing of a 5 mm circular transmural defect in a segment of an ex vivo porcine intestine (Figure 6a,b; and Movie S5, Supporting Information). To further simulate the stapler-based application in a minimally invasive surgical setting, sealing of an injured porcine intestine was repeated inside a dark chamber using a patch-loaded stapler inserted through ports and endoscopic camera footage to guide the process (Figure 6c; and Movie S5, Supporting Information). As represented by these ex vivo demonstrations, the multilayer patch can potentially serve as a primary sealing and repair modality for various organ defects. Alternatively, it can act as an adjunct on top of a suture or staple line to support an anastomosis, especially in patients at high risk of anastomotic failure.

In this work, we have introduced a versatile tissue sealing patch which is capable of achieving rapid and robust tissue adhesion in body fluid-rich environments and mitigating a range of perioperative and postoperative complications, such as infection, thrombus formation, and fibrotic encapsulations. While the full set of functionalities achieved by the multilayer patch make it an advantageous tissue sealant for surgery in general, its properties are particularly significant for use in minimally invasive surgery. Taking advantage of the material properties and paper-like form factor of the patch, we demonstrate that origami-based manufacturing techniques can

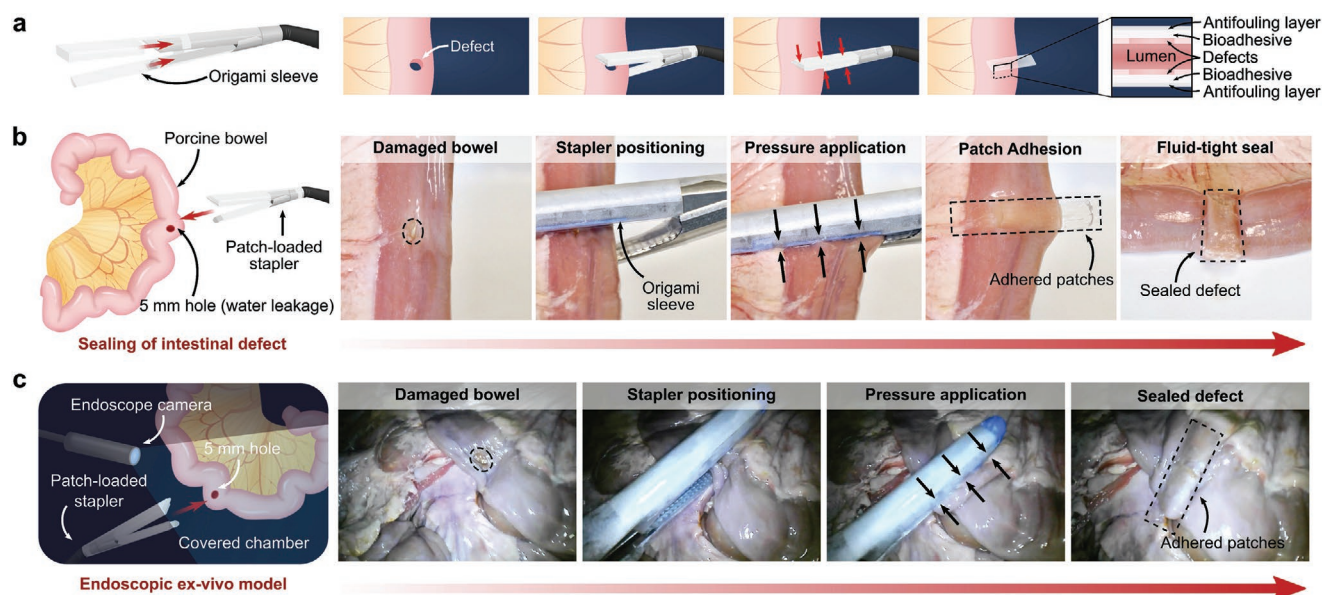


**Figure 6.** Ex vivo demonstrations of minimally invasive delivery and application of the multilayer bioadhesive patch to create using a surgical stapler. a) Schematic illustrations of the patch integration and delivery process using an articulating linear stapler. b) Macroscopic photographs of the fluid-tight linear sealing of a porcine intestinal defect (5-mm hole) by patches delivered and applied via an articulating linear stapler. c) Endoscopic footage of the sealing of a porcine intestinal defect (5-mm hole) performed in a dark, covered chamber to mimic a minimally invasive surgical procedure.

be adopted to integrate the patch with various surgical end effectors for deployment in diverse minimally invasive procedures. Given the versatility and unique bioadhesive capability of the multilayer patch, it holds the potential to overcome current translational barriers in surgery and facilitate the broader adoption of less damaging and less invasive surgical techniques.

## Experimental Section

**Preparation of the Bioadhesive Layer:** 30 w/w % acrylic acid, 2 w/w % chitosan (HMC+ Chitoscience Chitosan 95/500, 95% deacetylation), 1 w/w % acrylic acid *N*-hydroxysuccinimide ester, 0.2 w/w %  $\alpha$ -ketoglutaric acid, and 0.05 w/w % poly(ethylene glycol dimethacrylate) (PEGDMA;  $M_n = 550$ ) were dissolved in deionized water. For fluorescence microscopy visualization of the bioadhesive layer, fluorescein-labeled chitosan was used. The precursor solution was poured on a glass mold with spacers (the thickness is 210  $\mu$ m unless otherwise mentioned) and cured in a UV chamber (284 nm, 10 W power) for 30 min. Right after curing, dry bioadhesive microparticles were sifted through a 100  $\mu$ m sieve over the surface of the bioadhesive hydrogel. The resulting bioadhesive hydrogel with surface-embedded microparticles was then thoroughly dried and sealed in plastic bags with desiccant (silica gel packets) and stored at  $-20^\circ\text{C}$  prior to assembly with the nonadhesive layer.

**Preparation of the Bioadhesive Microparticles:** For fabrication of the bioadhesive microparticles, a bioadhesive film was first prepared by casting, curing, and drying the precursor solution described above. The fully dried bioadhesive material was then cryogenically grinded at 30 Hz frequency for 2 min. The resulting bioadhesive microparticles were sealed in plastic bags with desiccant and stored at  $-20^\circ\text{C}$  until use.

**Preparation of the Zwitterionic-Interpenetrated Elastomer:** 10 w/w % hydrophilic PU (HydroMed D3, Advansource Biomaterials) and 0.1 w/w % benzophenone dissolved in ethanol/water mixture (95:5 v/v) was spin-coated at 200 rpm. The spin-coated film was dried under airflow overnight, then submerged into an aqueous solution containing 35 w/w % [2-(methacryloyloxy)ethyl]dimethyl-(3-sulfopropyl)ammonium hydroxide (DMAPS) and 5 w/w %  $\alpha$ -ketoglutaric acid for 10 min, followed by curing in a UV chamber (284 nm, 10 W power) for 1 h. The resultant film was thoroughly washed in a large volume of deionized water for 3 days to remove unreacted reagents, then thoroughly dried under airflow.

**Assembly of the Multilayer Patch:** To combine the zwitterionic layer with the bioadhesive layer, a thin layer of 5 w/w % hydrophilic PU solution in ethanol/water mixture (95:5 v/v) was spin-coated at 400 rpm over the flat surface of the bioadhesive layer. The zwitterionic layer was then pressed on top and the entire assembly was thoroughly dried. The hydrophilic PU solution served as an adhesive between the zwitterionic layer and the bioadhesive layer by interpenetrating and drying between the two layers. To introduce the hydrophobic fluid layer, silicone oil (100 cSt viscosity) was first sterilized by filtration through a sterile membrane with 0.2  $\mu$ m pore size to remove bacteria and other microorganisms. The sterilized silicone oil was then impinged on the microtextured surface of the bioadhesive layer.

**Statistical Analysis:** MATLAB software was used to assess the statistical significance of all comparison studies in this work. Data distribution was assumed to be normal for all parametric tests, but not formally tested. In the statistical analysis for comparison between multiple samples, one-way ANOVA followed by Tukey's multiple comparison test were conducted with the threshold of  $*p \leq 0.05$ ,  $**p \leq 0.01$ , and  $***p \leq 0.001$ . In the statistical analysis between two data groups, a two-sample Student's *t*-test was used, and the significance threshold was placed at  $*p \leq 0.05$ ,  $**p \leq 0.01$ , and  $***p \leq 0.001$ .

**Animal Experiments:** All in vivo animal surgeries and ex vivo experiments were reviewed and approved by the Committee on Animal

Care at the Massachusetts Institute of Technology. Female Sprague–Dawley rats (Charles River Laboratories) were used for all in vivo studies. All porcine tissues and organs for ex vivo experiments (skin, trachea, aorta, esophagus, intestine) were purchased from a research-grade porcine tissue vendor (Sierra Medical, Inc.). Heparinized porcine blood was purchased from Lampire Biological Laboratories, Inc.

Other experimental details are included in Supporting Information.

## Supporting Information

Supporting Information is available from the Wiley Online Library or from the author.

## Acknowledgements

The authors thank Dr. X. Chen for the help on FTIR characterization, Y. Yang for the bacterial adhesion characterization, and the Koch Institute Swanson Biotechnology Center for technical support, specifically K. Cormier and the Histology Core for the histological processing; Funding: This work was supported by National Science Foundation (No. EFMA-1935291) and National Institutes of Health (No. 1R01HL153857-01). H.Y. acknowledges the financial support from Samsung Scholarship.

## Conflict of Interest

H.Y., S.W., C.S.N., and X.Z. are inventors of U.S. patent applications covering the origami multilayer bioadhesive patch and its minimally invasive surgery applications (U.S. Application No. U.S. No. 63/091076 and 63/091105).

## Author Contributions

S.J.W. and H.Y. contributed equally to this work. H.Y., S.W., and X.Z. conceived the idea and designed the study. H.Y. and S.W. developed the materials and method for the multilayer patch. H.Y., S.W., and C.S.N. designed the in vitro and ex vivo experiments. H.Y. and S.W. conducted the in vitro and ex vivo experiments. J.W. and H.Y. designed and conducted the in vivo experiments. S.W., H.Y., and X.Z. analyzed the results and wrote the manuscript with inputs from all authors.

## Keywords

antifouling materials, bioadhesives, minimally invasive surgery, origami-based manufacturing, wound sealing

Received: November 10, 2020

Published online:

- [1] FDA Executive Summary, prepared for the May 30, 2019 Meeting of the General and Plastic Surgery Devices Panel, *Reclassification of Surgical Staplers for Internal Use* **2019**, <https://www.fda.gov/media/126211/download>.
- [2] N. Annabi, K. Yue, A. Tamayol, A. Khademhosseini, *Eur. J. Pharm. Biopharm.* **2015**, 95, 27.
- [3] G. M. Taboada, K. Yang, M. Pereira, S. S. Liu, Y. Hu, J. M. Karp, N. Artzi, Y. Lee, *Nat. Rev. Mater.* **2020**, 5, 310.
- [4] Z. A. Murrell, M. J. Stamos, *Clin. Colon Rectal Surg.* **2006**, 19, 213.

- [5] D. N. Papachristou, J. G. Fortner, *Am. J. Surg.* **1979**, *138*, 399.
- [6] M. J. Mack, *JAMA, J. Am. Med. Assoc.* **2001**, *285*, 568.
- [7] R. K. Avery, H. Albadawi, M. Akbari, Y. S. Zhang, M. J. Duggan, D. V. Sahani, B. D. Olsen, A. Khademhosseini, R. Oklu, *Sci. Transl. Med.* **2016**, *8*, 365ra156.
- [8] J. Hu, I. Altun, Z. Zhang, H. Albadawi, M. A. Salomao, J. L. Mayer, L. P. Madhubhani, P. Hemachandra, S. Rehman, R. Oklu, *Adv. Mater.* **2020**, *32*, 2002611.
- [9] T. B. Reece, T. S. Maxey, I. L. Kron, *Am. J. Surg.* **2001**, *182*, S40.
- [10] M. Ryou, C. C. Thompson, *Tech. Gastrointest. Endosc.* **2006**, *8*, 33.
- [11] W. D. Spotnitz, S. Burks, *Transfusion* **2008**, *48*, 1502.
- [12] C. Cui, T. Wu, X. Chen, Y. Liu, Y. Li, Z. Xu, C. Fan, W. Liu, *Adv. Funct. Mater.* **2020**, *30*, 2005689.
- [13] H. Yuk, C. E. Varela, C. S. Nabzdyk, X. Mao, R. F. Padera, E. T. Roche, X. Zhao, *Nature* **2019**, *575*, 169.
- [14] Y. Wang, L. Shang, G. Chen, L. Sun, X. Zhang, Y. Zhao, *Sci. Adv.* **2020**, *6*, eaax8258.
- [15] A. Duarte, J. Coelho, J. Bordado, M. Cidade, M. Gil, *Prog. Polym. Sci.* **2012**, *37*, 1031.
- [16] R. D. O'Rourke, O. Pokholenko, F. Gao, T. Cheng, A. Shah, V. Mogal, T. W. J. Steele, *Biomacromolecules* **2017**, *18*, 674.
- [17] N. Lang, M. J. Pereira, Y. Lee, I. Friehs, N. V. Vasilyev, E. N. Feins, K. Ablasser, E. D. O'Cearbhaill, C. Xu, A. Fabozzo, R. Padera, S. Wasserman, F. Freudenthal, L. S. Ferreira, R. Langer, J. M. Karp, P. J. del Nido, *Sci. Transl. Med.* **2014**, *6*, 218ra6.
- [18] V. Bhagat, M. L. Becker, *Biomacromolecules* **2017**, *18*, 3009.
- [19] X. Chen, H. Yuk, J. Wu, C. S. Nabzdyk, X. Zhao, *Proc. Natl. Acad. Sci. USA* **2020**.
- [20] H. Yuk, J. Wu, X. Mao, C. E. Varela, E. T. Roche, C. S. Nabzdyk, X. Zhao, *bioRxiv* 2020.12.12.422505, **2020**; <https://doi.org/10.1101/2020.12.12.422505>.
- [21] A. K. Epstein, T. S. Wong, R. A. Belisle, E. M. Boggs, J. Aizenberg, *Proc. Natl. Acad. Sci. USA* **2012**, *109*, 13182.
- [22] S. Sunny, G. Cheng, D. Daniel, P. Lo, S. Ochoa, C. Howell, N. Vogel, A. Majid, J. Aizenberg, *Proc. Natl. Acad. Sci. USA* **2016**, *113*, 11676.
- [23] X. Mao, H. Yuk, X. Zhao, *J. Mech. Phys. Solids* **2020**, *137*, 103863.
- [24] H. Yuk, T. Zhang, S. Lin, G. A. Parada, X. Zhao, *Nat. Mater.* **2016**, *15*, 190.
- [25] S. Jiang, Z. Cao, *Adv. Mater.* **2010**, *22*, 920.
- [26] R. S. Smith, Z. Zhang, M. Bouchard, J. Li, H. S. Lapp, G. R. Brotske, D. L. Lucchino, D. Weaver, L. A. Roth, A. Coury, J. Biggerstaff, S. Sukavaneshvar, R. Langer, C. Loose, *Sci. Transl. Med.* **2012**, *4*, 153ra132.
- [27] L. Zhang, Z. Cao, T. Bai, L. Carr, J. Ella-Menye, C. Irvin, B. D. Ratner, S. Jiang, *Nat. Biotechnol.* **2013**, *31*, 553.
- [28] W.-W. Yue, H.-J. Li, T. Xiang, H. Qin, S.-D. Sun, C.-S. Zhao, *J. Membr. Sci.* **2013**, *446*, 79.
- [29] H. He, Z. Xiao, Y. Zhou, A. Chen, X. Xuan, Y. Li, X. Guo, J. Zheng, J. Xiao, J. Wu, *J. Mater. Chem.* **2019**, *7*, 1697.
- [30] J. Wu, W. Lin, Z. Wang, S. Chen, Y. Chang, *Langmuir* **2012**, *28*, 7436.
- [31] Y. Yu, H. Yuk, G. A. Parada, Y. Wu, X. Liu, C. S. Nabzdyk, K. Youcef-Toumi, J. Zang, X. Zhao, *Adv. Mater.* **2019**, *31*, 1807101.
- [32] L. Carr, G. Cheng, H. Xue, S. Jiang, *Langmuir* **2010**, *26*, 14793.
- [33] S. R. Myers, W. S. Rothermel, L. Shaffer, *Surgical Endoscopy* **2011**, *25*, 3043.
- [34] R. S. Baker, J. Foote, P. Kemmeter, R. Brady, T. Vroegop, M. Serveld, *Obesity Surgery* **2004**, *14*, 1290.
- [35] Y. Asada, A. Kisanuki, A. Tsuneyoshi, K. Marutsuka, K. Hatakeyama, A. Sumiyoshi, *Atherosclerosis* **1996**, *121*, 45.
- [36] D. C. Leslie, A. Waterhouse, J. B. Berthet, T. M. Valentin, A. L. Watters, A. Jain, P. Kim, B. D. Hatton, A. Nedder, K. Donovan, E. H. Super, C. Howell, C. P. Johnson, T. L. Vu, D. E. Bolgen, S. Rifai, A. R. Hansen, M. Aizenberg, M. Super, J. Aizenberg, D. E. Ingber, *Nat. Biotechnol.* **2014**, *32*, 1134.
- [37] B. Hellebrekers, T. Kooistra, *Br. J. Surg.* **2011**, *98*, 1503.
- [38] L. M. Stapleton, A. N. Steele, H. Wang, H. L. Hernandez, A. C. Yu, M. J. Paulsen, A. A. A. Smith, G. A. Roth, A. D. Thakore, H. J. Lucian, K. P. Theroow, S. W. Baker, Y. Tada, J. M. Farry, A. Eskandari, C. E. Hironaka, K. J. Jaatinen, K. M. Williams, H. Bergamasco, C. Marschel, B. Chadwick, F. Grady, M. Ma, E. A. Appel, Y. J. Woo, *Nat. Biomed. Eng.* **2019**, *3*, 611.
- [39] S. Miyashita, S. Guitron, S. Li, D. Rus, *Sci. Rob.* **2017**, *2*, eaao4369.
- [40] D. Rus, M. T. Tolley, *Nat. Rev. Mater.* **2018**, *3*, 101.
- [41] A. Rafsanjani, Y. Zhang, B. Liu, S. M. Rubinstein, K. Bertoldi, *Sci. Rob.* **2018**, *3*, eaar7555.



# ADVANCED MATERIALS

## Supporting Information

for *Adv. Mater.*, DOI: 10.1002/adma.202007667

### A Multifunctional Origami Patch for Minimally Invasive Tissue Sealing

*Sarah J. Wu, Hyunwoo Yuk,\* Jingjing Wu, Christoph S.  
Nabzdyk, and Xuanhe Zhao\**

Copyright Wiley-VCH GmbH, 2021.

## Supporting Information

### **Multifunctional Origami Patch for Minimally Invasive Tissue Sealing**

*Sarah J. Wu<sup>#</sup>, Hyunwoo Yuk<sup>#\*</sup>, Jingjing Wu, Christoph S. Nabzdyk, Xuanhe Zhao<sup>\*</sup>*

S. J. Wu, Dr. H. Yuk, Dr. J. Wu, Prof. X. Zhao  
Department of Mechanical Engineering, Massachusetts Institute of Technology, Cambridge,  
MA 02139, USA

\*E-mail: hyunwoo@mit.edu (H.Y.); zhaox@mit.edu (X.Z.)

Prof. C. S. Nabzdyk  
Department of Anesthesiology and Perioperative Medicine, Mayo Clinic, Rochester, MN 55905,  
USA

Prof. X. Zhao  
Department of Civil and Environmental Engineering, Massachusetts Institute of Technology,  
Cambridge, MA 02139, USA

<sup>#</sup>These authors contributed equally to this work.

**Supplementary Experimental Section**

*FTIR characterization:* Chemical composition of the zwitterionic-interpenetrated elastomer layer was characterized by a transmission Fourier transform infrared spectroscope (FTIR 6700, Thermo Fisher) using a Germanium attenuated total reflectance (ATR) crystal (55 deg).

*Microscope imaging:* Scanning electron microscope (SEM) images of the patch were taken by using an SEM facility (JSM-6010LA, JEOL) with 5 nm gold sputtering to enhance image contrasts. Confocal microscope images were obtained by an upright confocal microscope (SP8, Leica) with 490 nm excitation wavelength for fluorescein and 570 nm excitation wavelength for Rhodamine Red<sup>TM</sup>.

*Preparation of the gelatin hydrogel tissue phantom:* 10 w/w % gelatin (300 bloom) was dissolved in deionized water at 40 °C. The gelatin solution was then poured on a glass mold with 5 mm spacers. The gelatin hydrogel tissue phantoms were prepared by cooling the poured solution at room temperature for 1 h.

*Preparation of the pure zwitterionic hydrogel:* 50 w/w % DMAPS, 0.5% w/w % Irgacure 2959, and 0.5% w/w % PEGDMA were dissolved in deionized water. The precursor solution was then poured on a glass mold with 1 mm spacers. The zwitterionic hydrogels were cured in a UV chamber (284 nm, 10 W power) for 60 min.

*Quantification of blood entrapment:* A sample of the multilayer patch (25.4 mm in width and 25.4 mm in length) was prepared and coated with silicone oil (100 cSt viscosity). The multilayer patch then placed onto a gelatin hydrogel tissue phantom submerged in blood with the hydrophobic oil



layer facing downward. The multilayer patch was pressed against the tissue phantom at varying applied pressures using a mechanical testing machine (2.5 kN load-cell, Zwick/Roell Z2.5) for 5 s. The blood entrapped at the adhered patch-tissue phantom interface was visualized by taking photographs. To quantify the blood-entrapped area, the photographs were processed and analyzed by using ImageJ.

*Bacterial adhesion characterization:* An engineered *Escherichia coli* (*E. coli*) strain that constitutively expresses green fluorescent protein (GFP) was prepared by following the previously reported protocol and cultured in Luria-Bertani broth (LB broth) overnight at 37 °C. 1  $\mu$ L of bacteria culture diluted in 1 mL of fresh LB broth was placed on samples (1 cm  $\times$  1 cm) and incubated for 24 h at 37 °C.<sup>[31]</sup> After incubation, the samples were taken out and rinsed with phosphate buffered saline (PBS) to remove the free-floating bacteria, and imaged with a fluorescence microscope (Eclipse LV100ND, Nikon). The number of adhered *E. coli* on the samples per unit area (mm<sup>2</sup>) were counted by Image J.

*Fibrin deposition characterization:* A 5 v/v % solution of fetal bovine serum (FBS) in PBS used to block the wells of a 24-well plate for 30 min. The wells were rinsed with PBS, then 6 mm-diameter samples were placed in the blocked wells. The samples were submerged in porcine blood spiked with Alexa Fluor® 488-labeled human fibrinogen conjugate (66  $\mu$ g fibrinogen mL<sup>-1</sup> blood, Thermo Fisher) and incubated on a shaker in 220 rpm at room temperature for 60 min. The samples were gently rinsed in PBS and fixed for 1 hr in 2.5 v/v% glutaraldehyde in 0.1 M phosphate buffer. The samples were then imaged with a fluorescence microscope (Eclipse LV100ND, Nikon) and analyzed by using ImageJ.

*Mechanical characterization:* Unless otherwise indicated, the multilayer patch was applied by applying 77.5 kPa pressure for 5 s by a mechanical testing machine or equivalent weight. Unless otherwise indicated, all mechanical tests on adhesion samples were performed 6 h after initial pressing to ensure equilibrium swelling of the adhered multilayer patch in wet environments. The application of commercially-available tissue adhesives followed the provided manual for each product. Unless otherwise indicated, all adhesion characterization was performed on patches adhered to blood-covered tissues.

To measure interfacial toughness, adhered samples with widths of 2.5 cm were prepared and tested by the standard 180-degree peel test (ASTM F2256) using a mechanical testing machine (2.5-kN load-cell, Zwick/Roell Z2.5). All tests were conducted with a constant peeling speed of 50 mm min<sup>-1</sup>. The measured force reached a plateau as the peeling process entered the steady-state. Interfacial toughness was determined by dividing two times of the plateau force (for 180-degree peel test) with the width of the tissue sample (**Figure S12a**). Hydrophilic nylon filters (1 µm pore size, TISCH Scientific) were applied as a stiff backing for the multilayer patch. Poly(methyl methacrylate) (PMMA) films (with a thickness of 50 µm; Goodfellow) were applied using cyanoacrylate glue (Krazy Glue) as a stiff backing for the tissues.

To measure shear strength, the adhered samples with an adhesion area of 2.5 cm in width and 1 cm in length were prepared and tested by the standard lap-shear test (ASTM F2255) with a mechanical testing machine (2.5-kN load-cell, Zwick/Roell Z2.5). All tests were conducted with a constant tensile speed of 50 mm min<sup>-1</sup>. Shear strength was determined by dividing the maximum force by the adhesion area (**Figure S12b**). Hydrophilic nylon filters were applied as a stiff backing for the multilayer patch. PMMA films were applied using cyanoacrylate glue (Krazy Glue) as a stiff backing for the tissues.

To measure tensile strength, the adhered samples with adhesion area of 2.5 cm in width and 2.5 cm in length were prepared and tested by the standard tensile test (ASTM F2258) with the mechanical testing machine. All tests were conducted with a constant tensile speed of 50 mm min<sup>-1</sup>. Tensile strength was determined by dividing the maximum force with the adhesion area (**Figure S12c**). Aluminum fixtures were applied by using a cyanoacrylate glue to provide grips for the tensile tests.

The tensile properties and fracture toughness of the samples were measured using pure-shear tensile tests of thin rectangular samples (10 mm in length, 30 mm in width, and 0.5 mm in thickness) with a mechanical testing machine (20-N load-cell, Zwick/Roell Z2.5). All tests were conducted with a constant tensile speed of 50 mm min<sup>-1</sup>. The fracture toughness of the samples was calculated based on tensile tests of unnotched and notched samples (**Figure S5**).

*In vivo fibrous capsule characterization:* All animal surgeries were reviewed and approved by the Committee on Animal Care at the Massachusetts Institute of Technology. Female Sprague Dawley rats (225-250 g, Charles River Laboratories) were used for all *in vivo* studies. Before implantation, the multilayer patch was prepared using aseptic techniques and was further sterilized for 3 h under UV light. For implantation in the dorsal subcutaneous space, rats were anesthetized using isoflurane (1–2% isoflurane in oxygen) in an anesthetizing chamber. Anesthesia was maintained using a nose cone. The back hair was removed and the animals were placed over a heating pad for the duration of the surgery. The subcutaneous space was accessed by a 1-2 cm skin incision per implant in the center of the animal's back. To create space for implant placement, blunt dissection was performed from the incision towards the animal shoulder blades. multilayer patches with hydrophobic polymer (PDMS) faces ( $n = 4$ ), hydrophilic polymer (pristine hydrophilic PU) faces



( $n = 4$ ), and zwitterionic faces ( $n = 4$ ) with the size of 10 mm in width and 20 mm in length were placed in the subcutaneous pocket created above the incision without detachment. The incision was closed using interrupted sutures (4-0 Vicryl, Ethicon) and 3-6 ml of saline were injected subcutaneously. Up to four implants were placed per animal ensuring no overlap between each subcutaneous pocket created. After 2 or 4 weeks following the implantation, the animals were euthanized by CO<sub>2</sub> inhalation. Subcutaneous regions of interest were excised and fixed in 10% formalin for 24 h for histological analyses.

Fixed tissue samples were placed into 70% ethanol and submitted for histological processing and H&E and Masson's Trichrome staining at the Hope Babette Tang (1983) Histology Facility in the Koch Institute for Integrative Cancer Research at the Massachusetts Institute of Technology. The thickness of fibrous capsule was measured under a bright-field digital microscope (Eclipse LV100ND, Nikon) based on histology slides of each sample. Representative histology images of each group were shown in the corresponding figures.

*Ex vivo demonstrations:* All *ex vivo* experiments were reviewed and approved by the Committee on Animal Care at the Massachusetts Institute of Technology. All porcine tissues and organs for *ex vivo* experiments (skin, trachea, aorta, esophagus, intestine) were purchased from a research-grade porcine tissue vendor (Sierra Medical Inc.). Heparinized porcine blood was purchased from Lampire Biological Laboratories, Inc. For sealing of a tracheal defect, a 5 mm-diameter hole was punched to a porcine trachea with a biopsy punch. The upper portion of the trachea was connected to a tubing, through which air was pumped to inflate the lung lobes. A multilayer patch was folded into an origami sleeve and introduced to a Foley catheter (ReliaMed). The Foley catheter with the multilayer patch was inserted into the lumen of the damaged trachea. Once the multilayer patch

was located below the defect, the balloon was inflated to apply pressure to the multilayer patch against the walls of the trachea for 5 s to seal the defect. After sealing of the tracheal defect, air was pumped through the trachea to check the air-tight sealing of the trachea and restored inflation capability of the lung lobes.

For sealing of an esophageal defect, a 5 mm-diameter hole was punched in the wall of a porcine esophagus with a biopsy punch. Water was flowed through the esophagus at 100 mmHg using a tubing and a peristaltic pump (Thermo Fisher) to visualize leakage through the defect. A multilayer patch was folded into an origami sleeve and introduced to an esophageal catheter (Boston Scientific). The esophageal catheter with the multilayer patch was inserted into the lumen of the damaged esophagus. Once the multilayer patch was located below the defect, the balloon was inflated to apply pressure to the multilayer patch against the walls of the esophagus for 5 s to seal the defect. After sealing of the esophageal defect, water was pumped through the trachea to check the fluid-tight sealing of the esophagus.

For sealing of an aortic defect, a 5 mm-diameter hole was punched in the wall of a porcine aorta with a biopsy punch. Porcine blood was flowed through the esophagus at 120 mmHg using a tubing and a peristaltic pump (Thermo Fischer) to visualize leakage through the defect. A multilayer patch was folded into an origami sleeve and introduced to a Foley catheter (ReliaMed). The Foley catheter with the multilayer patch was inserted into the lumen of the damaged aorta. Once the multilayer patch was located below the defect, the balloon was inflated to apply pressure to the multilayer patch and the walls of the aorta for 5 s to seal the defect. After sealing of the aortic defect, porcine blood was pumped through the aorta to check the fluid-tight sealing of the aorta.

For sealing of an intestinal defect, a 5 mm-diameter hole was punched to a porcine small intestine with a biopsy punch. A patch-loaded origami sleeve was folded and introduced to an articulating linear stapler (Ethicon). The articulating linear stapler with the multilayer patch was endoscopically navigated to the defect site and actuated to apply compression for 5 s. The repaired intestine was connected to a pump and inflated to check for fluid-tight sealing of the bowel. To simulate a minimally invasive surgical setting, the experiment was repeated inside a dark chamber with holes, and a waterproof endoscope camera (DEPSTECH) was used for visualization.

Functional challenges for the minimally invasive delivery of surgical adhesives:

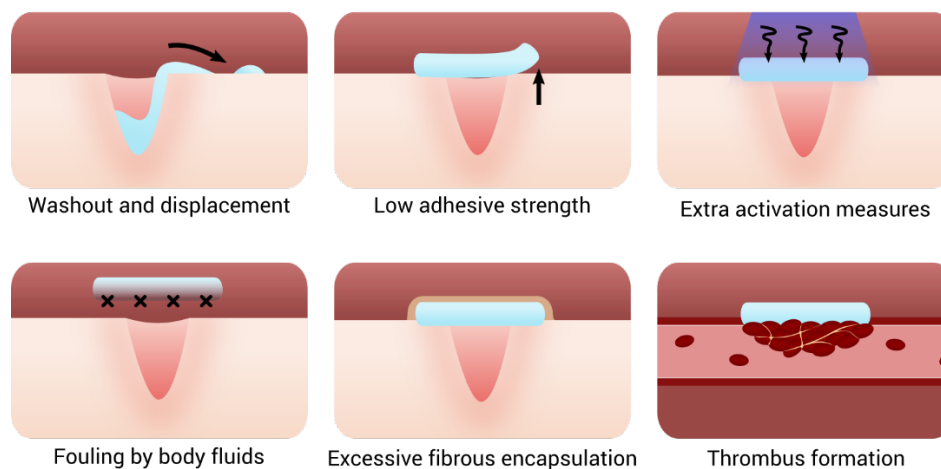


**Figure S1.** Functional limitations of existing bioadhesive materials for minimally invasive surgery.

Material & Form	Wet Tissue Adhesion	Body Fluid Resistance	Adhesion Speed	Adhesion Performance	Antifouling	MI Delivery & Application	Reference
Fibrin liquid glue	No	No	Slow (>3 min)	Low	No	Yes (injection)	FDA-approved product (Tisseel)
PEG liquid glue	No	No	Slow (>2 min)	Low	No	Yes (injection)	FDA-approved product (Coseal)
Cyanoacrylate liquid glue	No	No	Fast (<1 min)	High	No	N/R	FDA-approved product (Histoacryl)
Bulk tough hydrogel	Yes	Yes	Slow (>3 min)	High	No	No	<i>Science</i> <b>357</b> , 378 (2017)
Hydrophobic liquid glue	Yes	Yes	Slow (>2 min)	Intermediate	No	Yes (UV curing)	<i>Science Translational Medicine</i> <b>6</b> , 218ra6 (2014)
GelMA liquid glue	No	No	Slow (>2 min)	Intermediate	No	Yes (UV curing)	<i>Science Translational Medicine</i> <b>9</b> , eaai7466 (2017)
Double-sided tape	Yes	No	Fast (> 5 sec)	High	No	No	<i>Nature</i> <b>575</b> , 169-174 (2019)
Janus PACG & PACG-COS hydrogel patch	Yes	No	Fast (> 30 sec)	Intermediate	No	No	<i>Advanced Functional Materials</i> , 2005689 (2020)
Multilayer origami patch	Yes	Yes	Fast (>5 sec)	High	Yes	Yes	This work

\* N/R: Not reported.

**Supplementary Table 1.** Comparison of various bioadhesives and their functional performance for minimally invasive surgery.



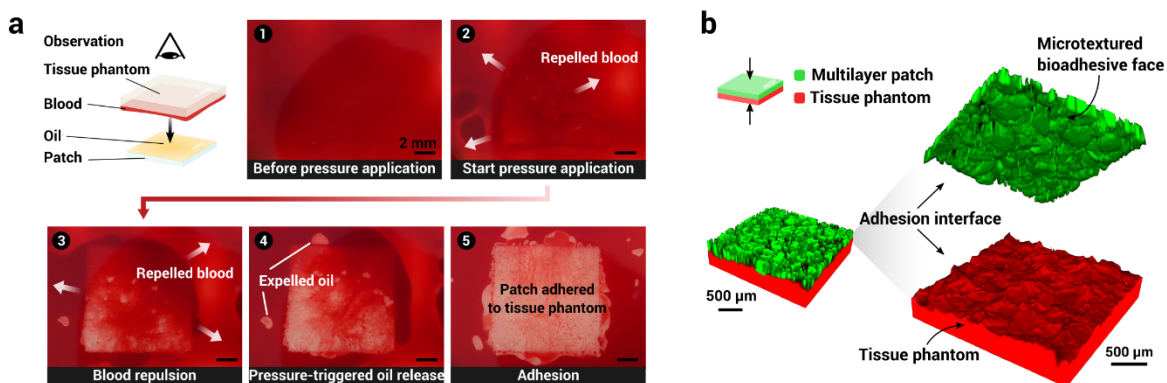


**Figure S2.** a) Photographs of the blood repellence and adhesion formation process between a multilayer patch and a gelatin hydrogel tissue phantom. b) 3D reconstruction of confocal micrographs at the interface of adhesion between the micro-textured bioadhesive face (green) and a tissue phantom of gelatin hydrogel (red).

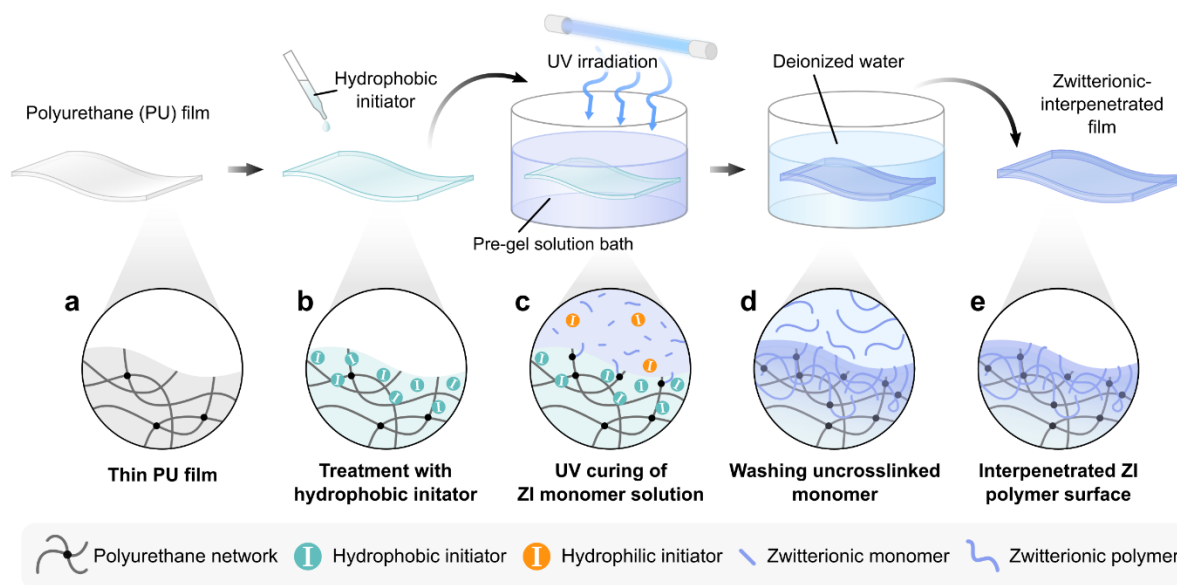


**Figure S3.** Preparation of the zwitterionic-interpenetrated elastomer antifouling layer. a-b) A thin film of hydrophilic PU is treated with a hydrophobic initiator (i.e., benzophenone). c) The treated hydrophilic PU film is submerged in a precursor solution containing the zwitterionic monomer and hydrophilic initiator (i.e.,  $\alpha$ -ketoglutaric acid), then cured in a UV chamber. d) The sample is washed in a large volume of deionized water. e) A zwitterionic-interpenetrated polyurethane film is retrieved.

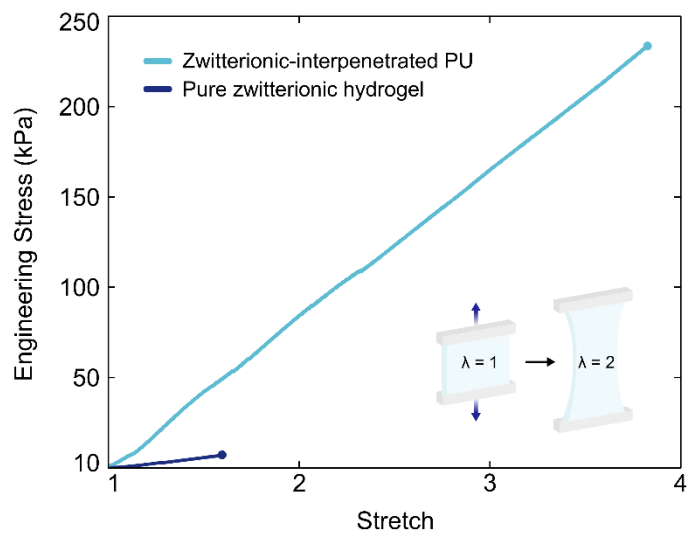


**Figure S4.** Representative engineering stress vs. stretch curves for the zwitterionic-interpenetrated polyurethane layer and a pure zwitterionic hydrogel.

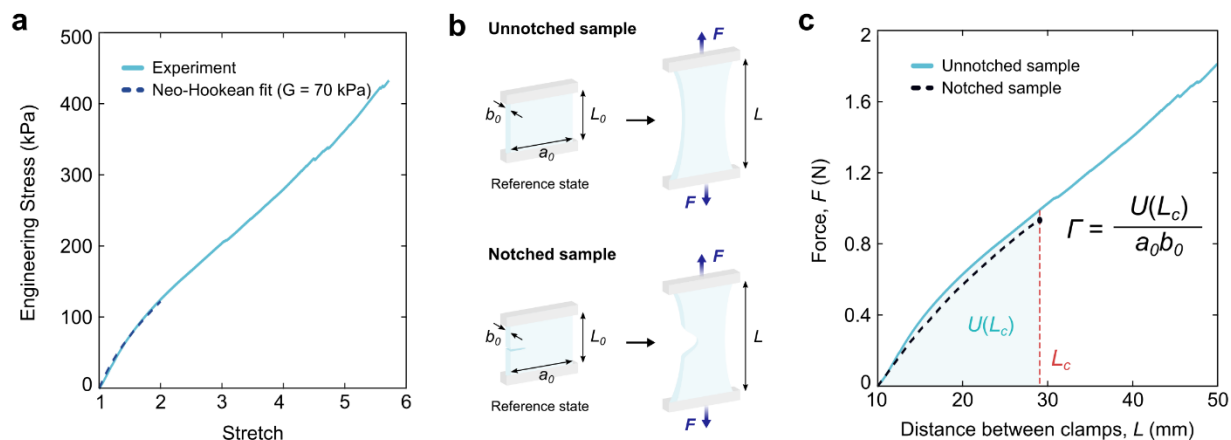


**Figure S5.** Mechanical characterization of the multilayer patch. a) Engineering stress vs. stretch curve of the multilayer patch. The measured shear modulus of the multilayer patch is 70 kPa. c) Schematic illustrations of a pure-shear test for unnotched and notched samples. c) Force vs. distance between clamps curves for the unnotched and notched antifouling face.  $L_c$  indicates the critical distance between the clamps at which the notch turns into a running crack. The measured fracture toughness of the multilayer patch is  $2,100 \text{ J m}^{-2}$ .

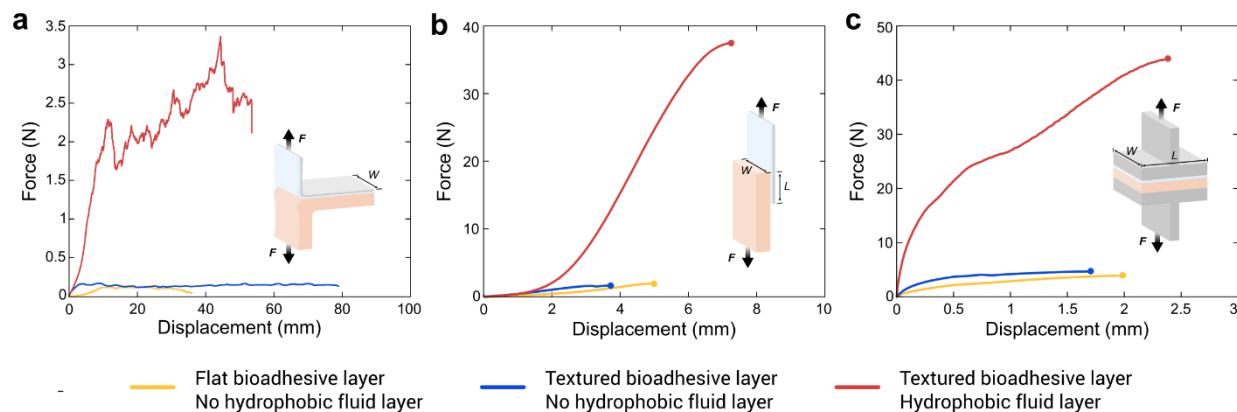


**Figure S6.** Representative force vs. displacement curves for a) 180-degree peel tests, b) lap-shear tests, and c) tensile tests of various multilayer patches adhered on blood-covered porcine skin. All patches were adhered to the tissue substrates by applying 77.5 kPa of pressure for 5 s.



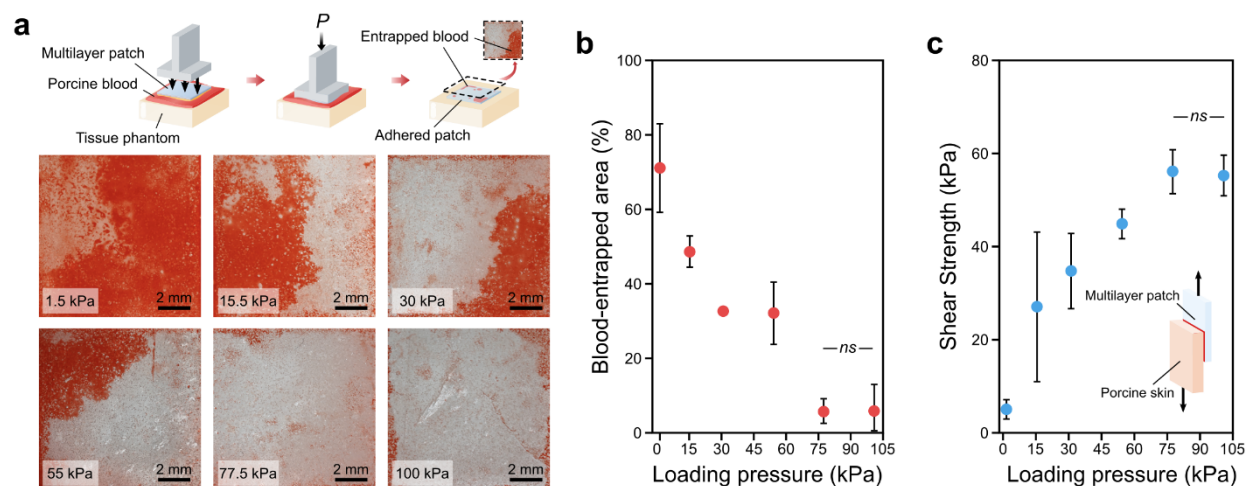


**Figure S7.** Characterization of blood repellence and adhesion performances of the multilayer patch under varying applied pressures. a) Representative photographs of the interfaces between the adhered multilayer patches and tissue phantom gelatin hydrogels. b) Percentage of blood-entrapped area at the interface as a function of applied pressure. c) Shear strength of adhered multilayer patches and blood-covered porcine skin as a function of applied pressure. Values in (b,c) represent the mean and the standard deviation ( $n = 2$ ).  $P$  values are determined by a Student's  $t$ -test; \*  $p \leq 0.05$ ; \*\*  $p \leq 0.01$ ; \*\*\*  $p \leq 0.001$ .

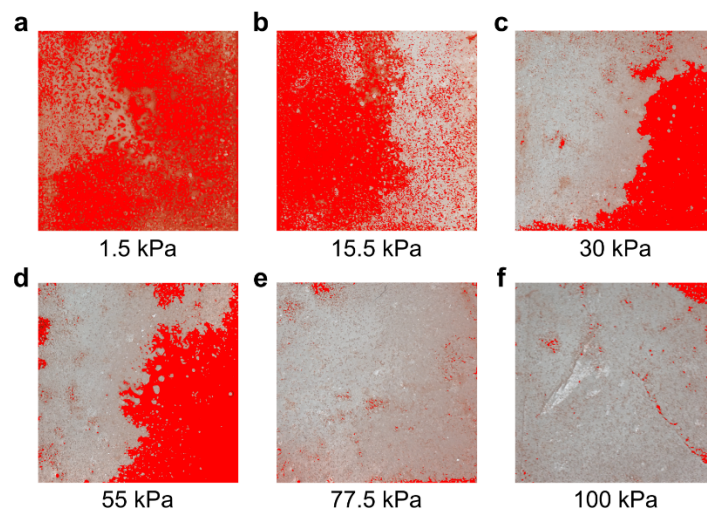


**Figure S8.** Representative processed images for the quantification of blood entrapment at the area of adhesion between the multilayer patches and blood-covered gelatin hydrogel tissue phantom compressed at 1.5 kPa (a), 15.5 kPa (b), 30 kPa (c), 55 kPa (d), 77.5 kPa (e), and 100 kPa (f) for 5 s. Photographs were processed by globally thresholding in ImageJ, then analyzed to quantify the percentage of blood-entrapped area.

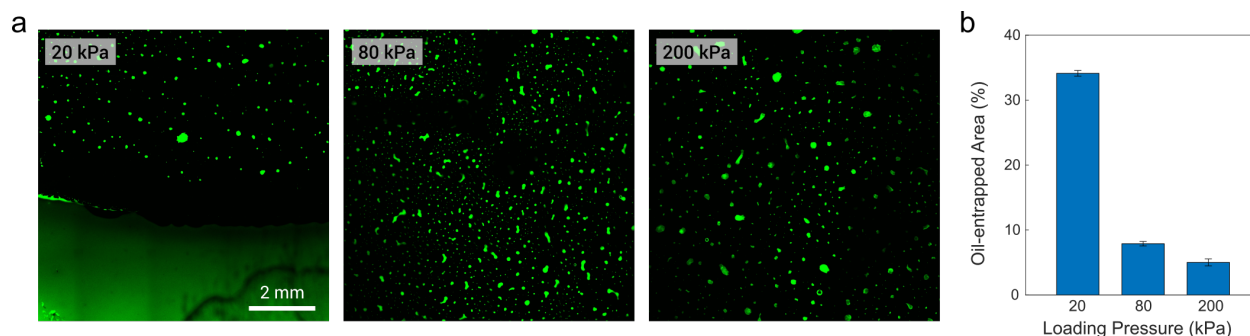


**Figure S9.** Interfacial oil entrapment as a function of applied pressure. a) Representative fluorescence micrographs of the adhesion interface between the bioadhesive patch and a gelatin tissue phantom substrate adhered under pressures of 20, 80, and 200 kPa. Residual fluorescently-dyed silicone oil can be visualized using fluorescent microscopy. b) Percentage of oil-entrapped area at the interface for loading pressures of 20, 80, and 200 kPa. The percentages of oil-entrapped area were  $34.1 \pm 0.4\%$ ,  $7.9 \pm 0.3\%$ , and  $5.0 \pm 0.5\%$ , respectively. Values represent the mean and standard deviation ( $n = 3$ ).

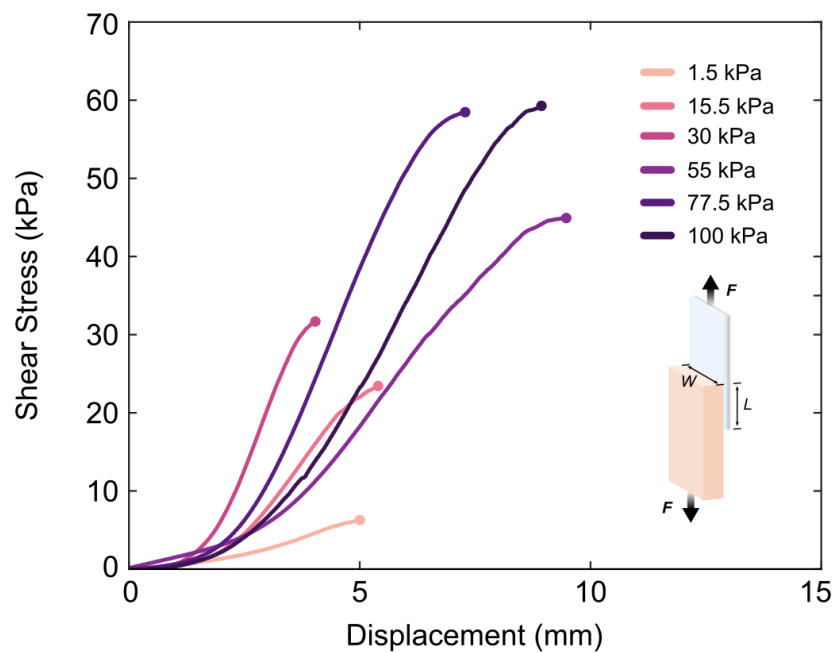


**Figure S10.** Shear stress vs. displacement curves for lap-shear tests of multilayer patches adhered to blood-covered porcine skins with varying applied pressures (1.5, 15.5, 30, 55, 77.5, and 100 kPa) for 5 s.

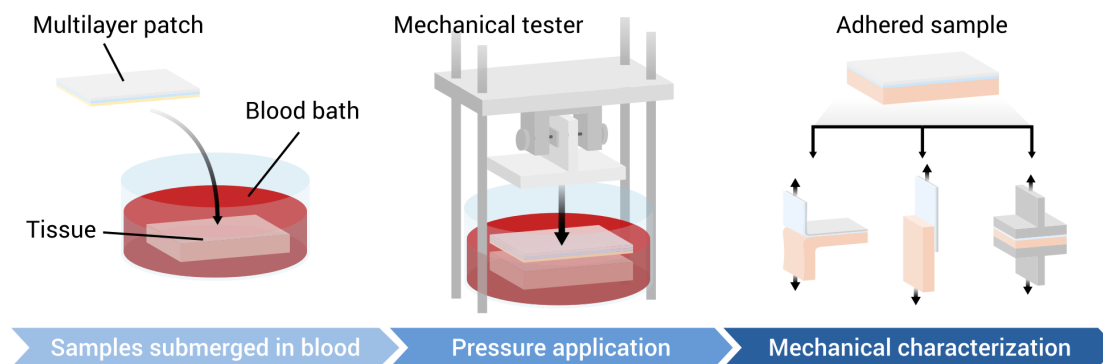


**Figure S11.** Experimental setup for the adhesion characterization of the multilayer patch and tissues submerged in blood. First, a sample of porcine tissue is covered with heparinized porcine blood. The multilayer patch is placed in the blood bath, then a mechanical tester applies a controlled pressure to adhere the patch to the tissue. After 5 s of pressure application, the adhered sample is collected for mechanical characterization to measure interfacial toughness, shear strength, or tensile strength, following ASTM standards F2256, F2255, and F2258.



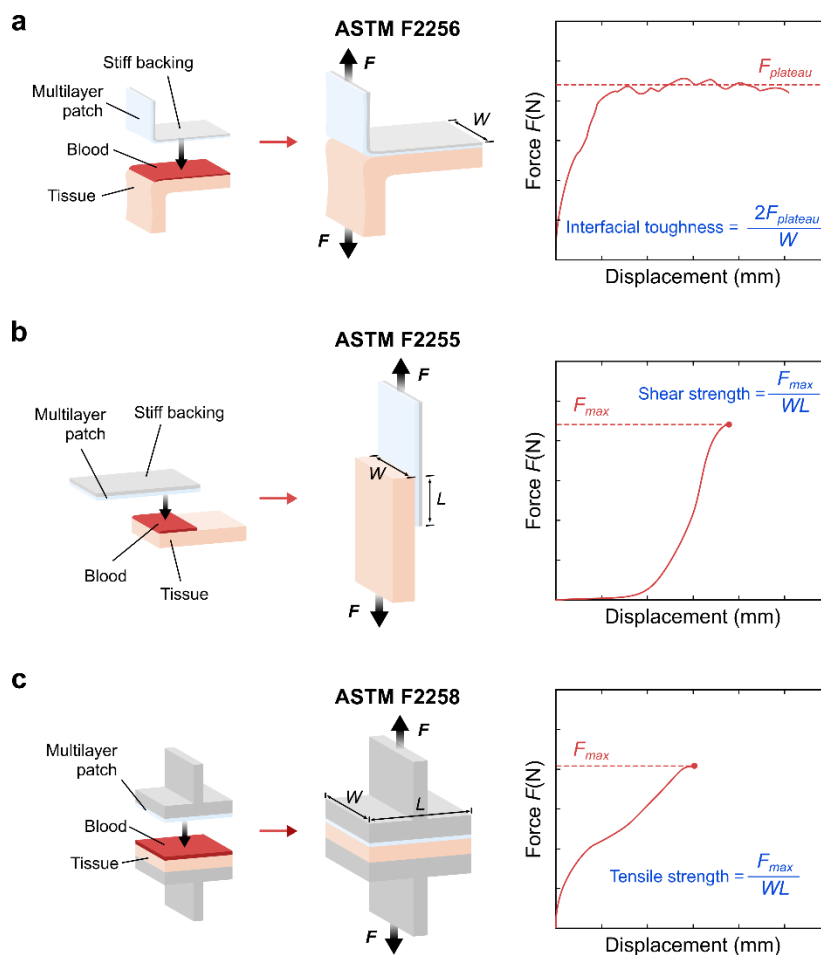


**Figure S12.** a) Schematic illustrations of the experimental setup for interfacial toughness measurements based on the standard 180-degree peel test (ASTM F2256). b) Schematic illustrations of the experimental setup for shear strength measurements based on the standard lap-shear test (ASTM F2255). c) Schematic illustrations of the experimental setup for tensile strength measurements based on the standard tensile test (ASTM F2258).

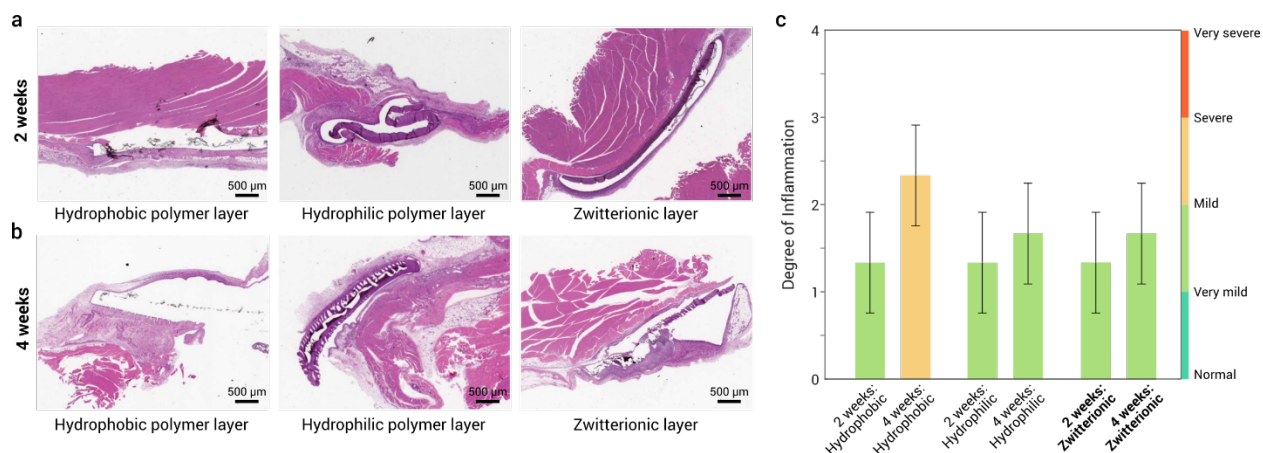


**Figure S13.** *In vivo* biocompatibility of the multilayer patch. Representative H&E histological images of multilayer patches with non-adhesive layers comprised of a hydrophobic polymer, a hydrophilic polymer, and a zwitterionic-interpenetrated elastomer layer implanted into the dorsal subcutaneous spaces of rats after a) 2 weeks and b) 4 weeks. c) Histological evaluation of the degree of inflammation at the implantation sites by a blinded pathologist. Degree of inflammation is scored wherein 0 = normal, 1 very mild, 2 = mild, 3 = severe, and 4 = very severe. Values represent the mean and standard deviation ( $n = 3$ ).

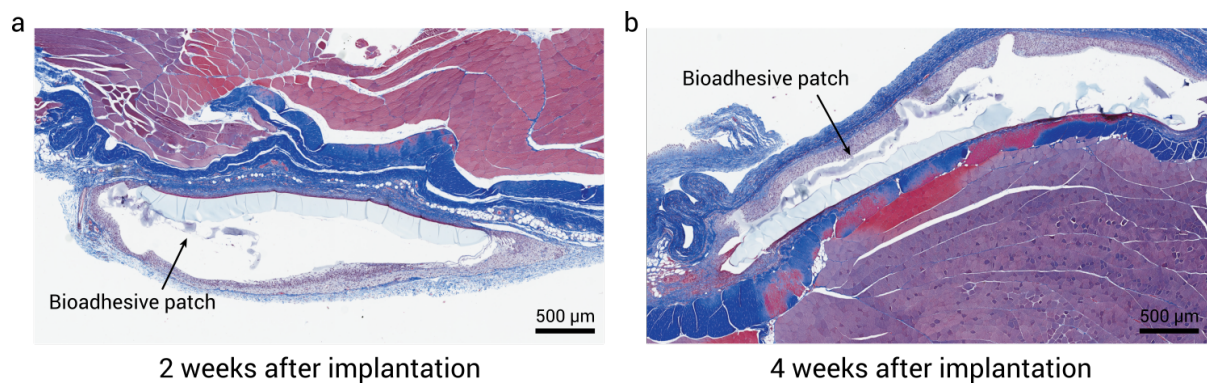


**Figure S14.** *In vivo* stability of the multilayer patch. Representative histological images stained with Masson's trichrome of samples implanted into the dorsal subcutaneous spaces of rats for a) 2 weeks and b) 4 weeks. At 4 weeks after implantation, the bioadhesive patch exhibits gradual degradation and decomposition.

## **Movie S1**

Robust blood resistance of the multilayer patch against vigorous agitations in a porcine blood bath.

## **Movie S2**

Minimally invasive delivery and sealing of an *ex vivo* porcine trachea by the multilayer patch.

## **Movie S3**

Minimally invasive delivery and sealing of an *ex vivo* porcine esophagus by the multilayer patch.

## **Movie S4**

Minimally invasive delivery and sealing of an *ex vivo* porcine aorta by the multilayer patch.

## **Movie S5**

Minimally invasive delivery and sealing of an *ex vivo* porcine intestine by the multilayer patch.